OUKA
The University of Osaka
Institutional Knowledge Archive

Title	Structure of chloramphenicol-bound MexB reveals residues in the distal binding pocket that are critical for substrate recognition
Author(s)	上田, 雄士
Citation	大阪大学, 2026, 博士論文
Version Type	VoR
URL	https://doi.org/10.18910/105664
rights	
Note	

The University of Osaka Institutional Knowledge Archive : OUKA

https://ir.library.osaka-u.ac.jp/

The University of Osaka

Structure of chloramphenicol-bound MexB reveals residues in the distal binding pocket that are critical for substrate recognition

（クロラムフェニコール結合MexBの構造から明らかにされた基質認識に重要な遠位結合ポケットのアミノ酸残基）

A doctoral thesis

By

Yushi Ueda

Submitted to

The Graduate School of Science, The University of Osaka

January 2026

Acknowledgements

This study was conducted in the Laboratory for Supramolecular Crystallography, Institute for Protein Research, Osaka University. First and foremost, I would like to express my sincere gratitude to my supervisors, Professor Atsushi Nakagawa and Associate Professor Eiki Yamashita, for their continuous guidance, encouragement, and unwavering support throughout my research.

I am also deeply grateful to Professor Junichi Takagi of the Institute for Protein Research, Osaka University, and Professor Takahide Kon of the Graduate School of Science, Osaka University, for their careful and thorough review of my doctoral thesis and for providing constructive and insightful comments.

I would like to extend my heartfelt thanks to Dr. Ryo Yonehara for providing the analytical data for drug-free MexB, and to Dr. Etsuko Ikeda (Ishizaka) for conducting analyses of several MexB variants.

I am further grateful to the anonymous reviewers and the editor of our submitted manuscript. Without their support and valuable feedback, I would not have been able to even prepare for the doctoral thesis examination.

I would also like to thank all past and present members of the Laboratory of Supramolecular Crystallography for their helpful advice and daily support in my research life. I am equally grateful to my friends who walked alongside me throughout the doctoral program. Finally, I would like to express my deepest appreciation to everyone in the laboratory for their warm support and friendship during my Ph.D. course.

Yushi Ueda

January 2026

Chapter1

Introduction

1.1 A Multidrug resistance of *Pseudomonas aeruginosa*

1.2 RND-type multidrug efflux pump MexAB-OprM

1.3 RND transporter MexB

1.4 Purpose of this study

Chapter2

The structure of drug-free MexB

2.1 Material and Methods

2.2 Result

Chapter3

The structure of antibiotics-bound MexB

3.1 Material and Methods

3.2 Result

Chapter4

In vivo drug resistance assay of cells harboring deep binding pocket variants.

4.1 Material and Methods

4.2 Result

Chapter5

Discussion and conclusion

5.1 Discussion

5.2 Conclusion

5.3 Reference

5.4 Publication

1. Introduction

1.1 A Multidrug resistance of *Pseudomonas aeruginosa*

Pseudomonas aeruginosa is a representative opportunistic pathogen that exhibits multidrug resistance and causes severe infections, particularly in immunocompromised patients (1). This bacterium has acquired resistance to multiple antimicrobial agents, largely because it possesses tripartite multidrug efflux pumps belonging to the resistance–nodulation–division (RND) superfamily, which form a continuous conduit across the inner and outer membranes and expel antibiotics (2) (Fig.1.1.1). These tripartite efflux systems consist of an inner-membrane RND transporter that functions as a proton/drug antiporter (3), an outer membrane channel (outer membrane factor, OMF) (4), and a periplasmic adaptor protein (PAP) that bridges the RND transporter and the OMF (5).

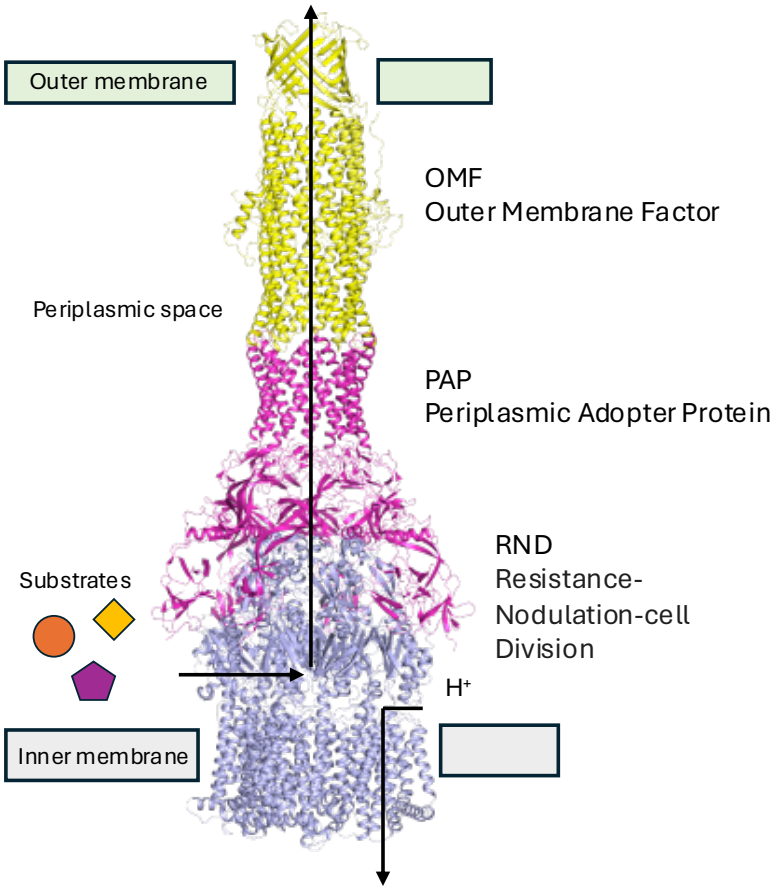

Fig.1.1.1 Schematic diagram of the tripartite structure of the resistance-nodulation-division (RND) superfamily.

The complex consists of three components: OMF (Outer membrane factor), RND (Resistance nodulation-cell division) transporter, and PAP (periplasmic adaptor protein).

1.2 RND-type multidrug efflux pump MexAB-OprM

In *P. aeruginosa*, the most abundantly expressed RND-type efflux pump complex is MexAB–OprM (Fig. 1.1.1) (6), which exports as substrates a wide range of antibiotics with diverse molecular weights and structures, as well as detergents and dyes (7–9).

MexAB–OprM is composed of an outer membrane factor (OMF; OprM) (Fig.1.2.1C) that forms a trimer in the outer membrane (4,10), an RND-type multidrug efflux transporter (MexB) that forms a trimer in the inner membrane (3,11) (Fig.1.2.1A), and a periplasmic adaptor protein (PAP; MexA) (Fig.1.2.1B) that assembles as a hexamer bridging these components (5,12). Among these components, the multidrug efflux transporter MexB plays a pivotal role in this complex by recognizing substrates (Fig. 1.2.2).

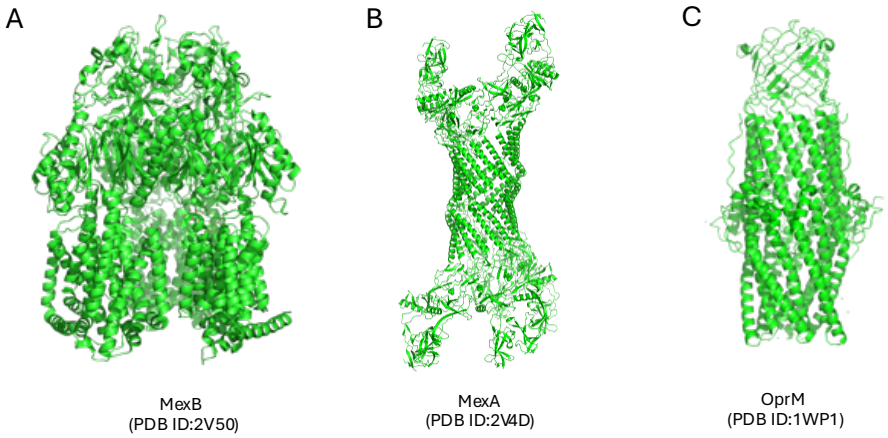

Fig.1.2.1 Structure of each protein that makes up MexAB-OprM.

(A) Crystal structure of MexB (PDB ID:2V50)

(B) Crystal structure of MexA (PDB ID:2V4D)

(C) Crystal structure of OprM (PDB ID:1WP1)

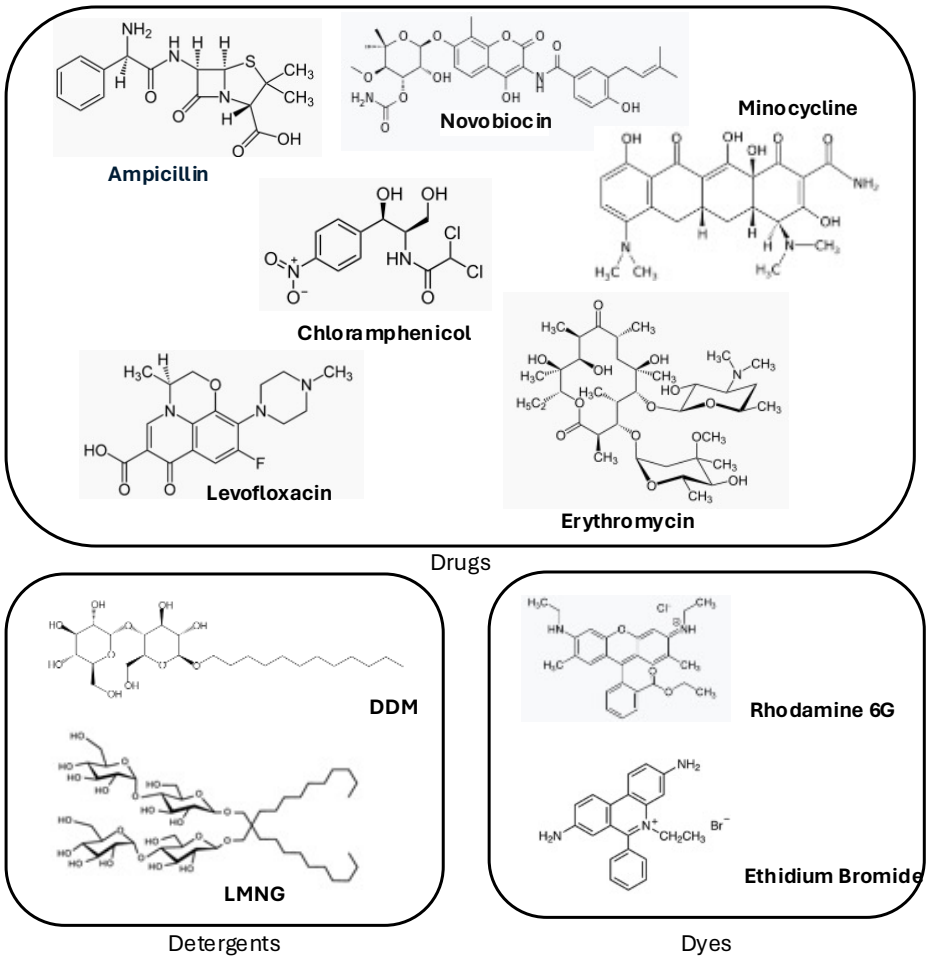

Fig. 1.2.2 Examples of compounds that serve as substrates for MexB.

1.3 RND transporter MexB

Among RND transporters, AcrB from *Escherichia coli* and MexB from *P. aeruginosa* are two of the best-characterized representatives. Structural and functional studies on these pumps have converged on a shared mode of action (11, 13). Both proteins operate as homotrimers: within the membrane, the three protomers adopt three distinct conformational states—commonly termed Access, Binding, and Extrusion—and, driven by the proton-motive force, interconvert sequentially between these states (Fig.1.3.1). Through this conformational cycling, the pumps are thought to capture substrates and expel them efficiently from the cell (13).

Each protomer is organized into three major domains: a periplasmic funnel-like (FL) domain, a porter domain, and a transmembrane (TM) domain (13) (Fig.1.3.2). The TM domain comprises 12 helices (TM1–TM12) and harbors key residues required for proton translocation, notably conserved aspartate residues in TM4 and a lysine residue in TM10. Mutations at these positions abolish efflux activity, indicating that they are essential for the proton-relay network that fuels transport (14). In the Access and Binding conformations, the aspartate and lysine residues interact via a salt bridge, whereas in the Extrusion state the lysine side chain instead contacts a conserved threonine in TM11 (11, 13) (Fig.1.3.3).

The porter domain is subdivided into four subdomains, PN1, PN2, PC1, and PC2 (Fig. 1.3.4A). In the Access state, the PN1–PN2 gate is closed and the PC1–PC2 gate is open, allowing substrates to enter from the periplasm. In the Binding state, the PN1–PN2 gate remains shut, while the PC1–PC2 gate opens further to generate an internal binding site.

In the Extrusion state, opening of the PN1–PN2 gate and closure of the PC1–PC2 gate direct the substrate captured in the Binding state into the central channel of the trimer (13) (Fig.1.3.4B). More recently, a fourth "resting" conformation, in which both PN1–PN2 and PC1–PC2 gates are closed, has been proposed to represent an off-cycle, inactive state of the transporter (15, 16). Within the porter domain, two binding pockets have been identified—the proximal binding pocket (PBP) (11) and the distal binding pocket (DBP) (17) (Fig. 1.3.5)—which are thought to contribute differentially depending on substrate size and type (17). Substrates reach these pockets through four channels, CH1–CH4, formed by elements of both the TM and porter domains (11, 13, 17, 18, 19, 20) (Fig. 1.3.6). Structural and functional analyses indicate that which channel is used depends on the physicochemical properties of the substrate (17, 20).

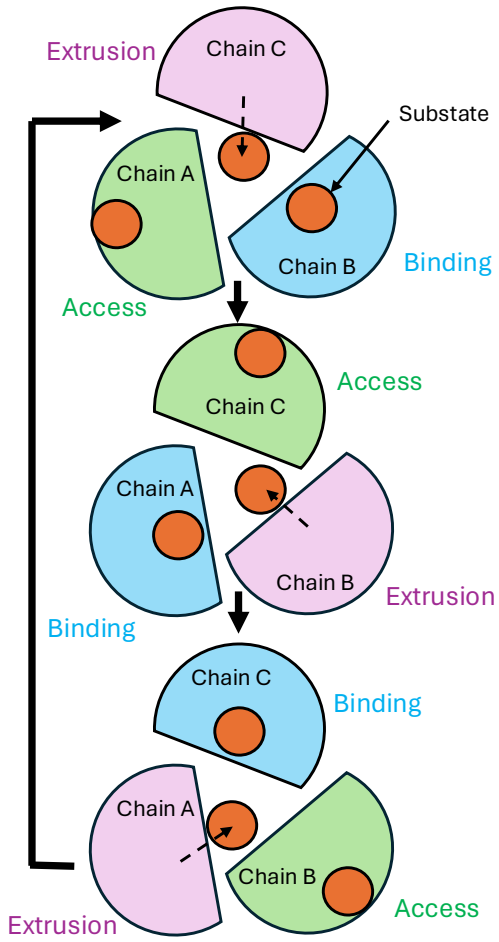

Fig.1.3.1 Overview of the functional rotation mechanism in RND transporters.

Green indicates Access, blue indicates Binding, and red indicates Extrusion. Drugs taken in through Access are bound to the deep pockets of Binding, and in the Extrusion state are expelled through the central pore.

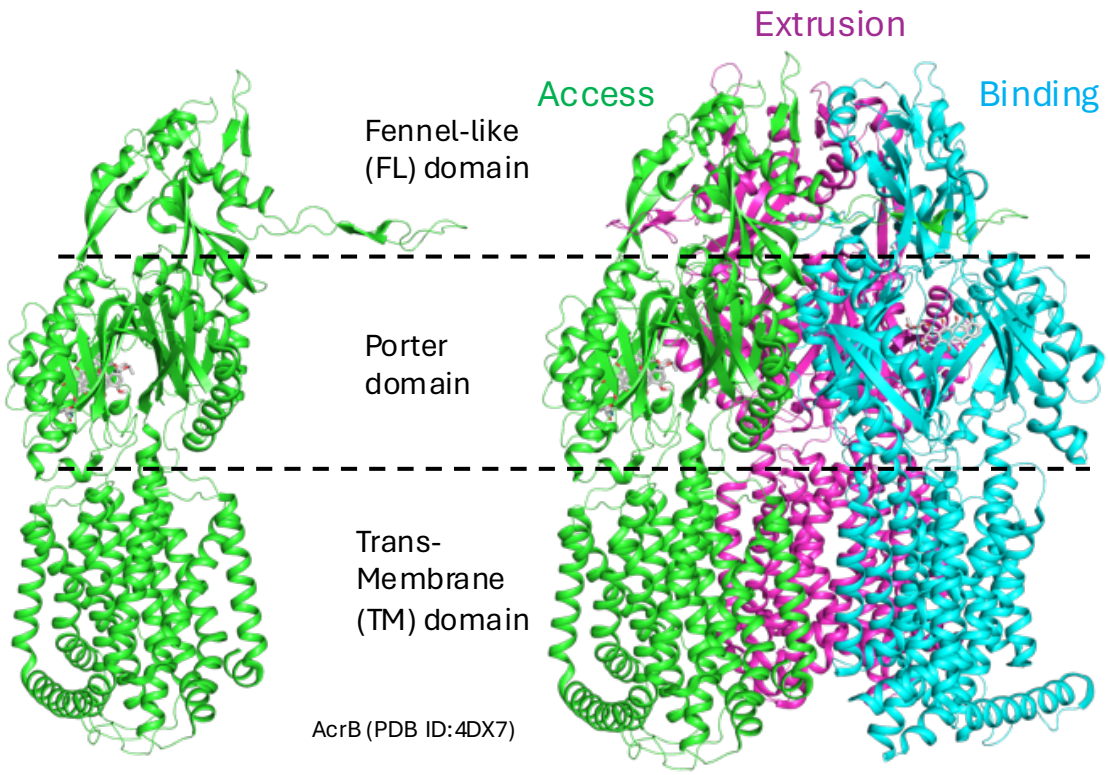

Fig.1.3.2 Three domains of the RND transporter.

Lateral view of the RND transporter relative to the plasma membrane.

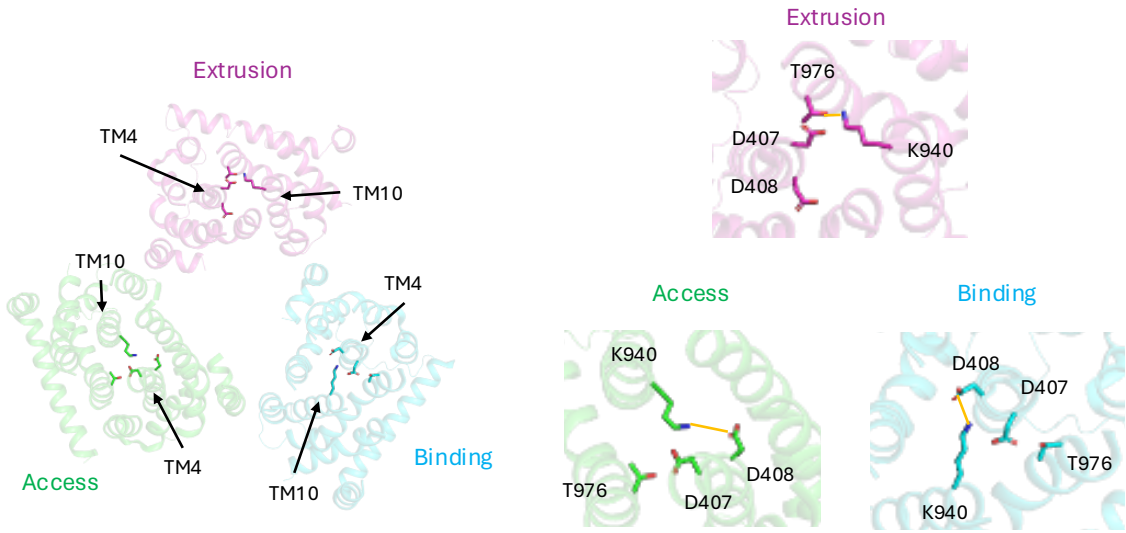

Fig.1.3.3 Comparison of amino acid residues involved in proton transport in each state (access, binding, extrusion).

Each chain is displayed as a cartoon model, and only the residues involved in proton transport are shown as stick models.

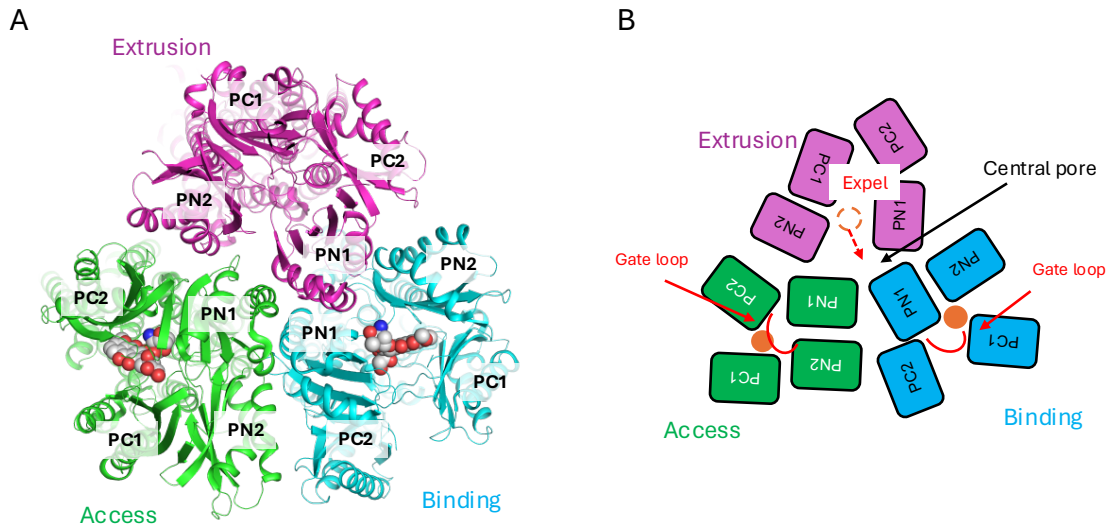

Fig. 1.3.4 The porter subdomains that make up the porter domain (

(A) Top view of porter domain. PN1, PN2, PC1, and PC2 are displayed on each chain.

(B) The schematic diagram of the porter domain

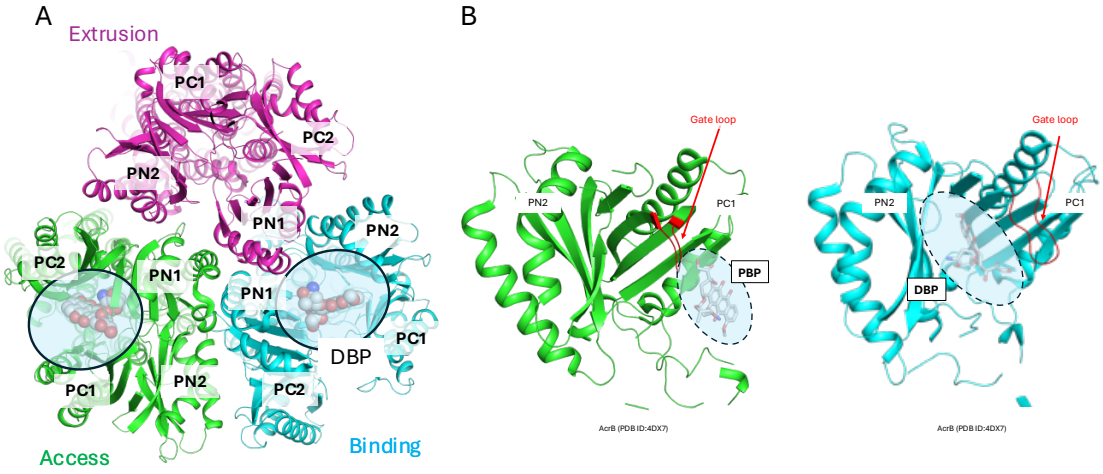

Fig. 1.3.5 Positional relationship between PBP and DBP

(A) Top view of porter domain and the relative positions of PBP and DBP

(B) PBP is in front of the gate loop, and DBP is located behind the gate loop.

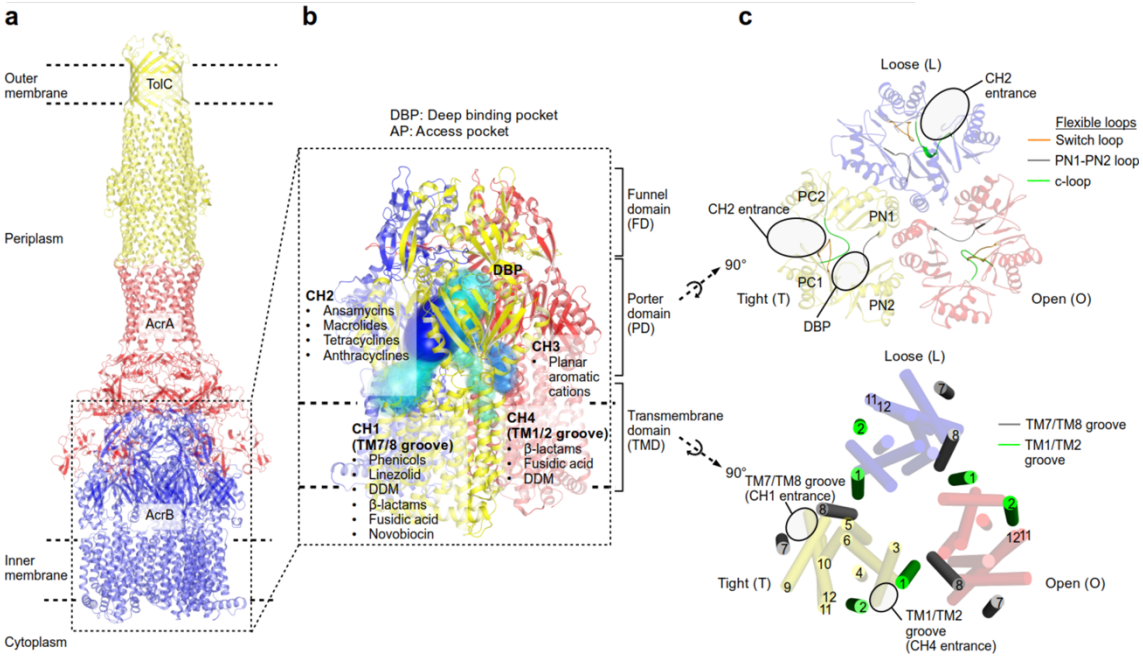

Fig.1.3.6 Channels (*20*) (CH1-4) proposed from the AcrB crystal structure

Putative AcrB substrate transport pathways (CH1-4) and substrate specificity of each channel inferred from drug resistance experiments using mutants.

1.4 Purpose of this study

MexB is known to extrude a broad spectrum of compounds, including β-lactams, fluoroquinolones, macrolides, tetracyclines, and chloramphenicol. However, no structure of MexB in complex with an antibiotic substrate has yet been described. To date, structural information on MexB has come from X-ray crystallography (11, 21, 22) and cryo-electron microscopy (23), which have revealed detergent-bound forms, inhibitor-bound forms, and apo structures only. Consequently, the substrate-recognition mechanism of MexB remains unresolved at the structural level.

In this study, to gain a more comprehensive understanding of how MexB recognizes chemically diverse substrates, we took advantage of a newly established mildly basic crystallization condition for MexB. Using this approach, we determined the structures of drug-free MexB and drug-bound MexB.

2 The structure of drug-free MexB

Two crystal structures of MexB have been reported previously; however, no structure of MexB in complex with an antibiotic has been described. We also attempted to crystallize MexB and obtain substrate-bound structures using similar acidic conditions but were unable to determine any substrate-bound MexB structure. To facilitate the determination of multiple substrate-bound MexB structures, we therefore established two new crystallization conditions: one mildly basic and the other mildly acidic. High-resolution diffraction data were obtained from crystals grown under both conditions. Among these, we determined the structure of MexB from crystals grown under the mildly basic condition. In this structure, MexB forms a homotrimer in which the three protomers adopt distinct Access, Binding, and Extrusion conformations. The detergent CYMAL-7, which was also used during purification, was observed bound in the substrate-binding pocket of the Binding protomer.

2.1 Material and Methods

2.1.1 Transformation and MexB expression

The expression vector pET22b(+)-*mexB* was transformed into *E coli* C43(DE3). Transformants were spread on Luria–Bertani (LB) agar plates containing 100 μg/mL ampicillin and incubated at 37°C for 16 h. A single colony was inoculated into 3 mL LB medium containing 100 μg/mL ampicillin and cultured at 37°C with shaking at 135 rpm for 16 h. This preculture was transferred to 200 mL Terrific Broth (TB) medium containing 100 μg/mL ampicillin and incubated at 37°C with shaking at 180 rpm for 4 h. The resulting culture was added to 10 L TB medium containing 50 μg/mL ampicillin and incubated at 37°C with shaking at 270 rpm until the optical density at 600 nm (OD600) reached 0.3–0.4. Protein expression was induced by adding isopropyl β-D-1-thiogalactopyranoside (IPTG) to a final concentration of 120 μM, followed by incubation at 20°C with shaking at 270 rpm for approximately 22 h.

Cells were harvested using an Avanti HP-20 XP centrifuge (Beckman Coulter) equipped with a JLA-8.1000 rotor at 20°C and 5,000 × g for 10 min. The cell pellet was resuspended in phosphate-buffered saline (PBS; 50 mM sodium phosphate, pH 7.4, 100 mM NaCl), transferred to 50 mL tubes, and centrifuged at 20°C and 10,000 × g for 10 min. The resulting cell pellets were collected and stored at −30°C until use.

2.1.2 Membrane preparation

The frozen cell was resuspended in buffer A (50 mM sodium phosphate, pH 7.4, 100 mM NaCl, 2 mM $MgCl_2$, 10 µg/mL DNase I) at a ratio of 200 mL buffer per 220 g cells, and the suspension was passed through a high-pressure cell disruptor APV-1000 (SPX Corporation) at 850–900 bar for 5 min. This procedure was repeated three times to lyse the cells. The cell lysate was centrifuged at 10,000 × g for 10 min at 4°C, and the supernatant containing the membranes was collected and subjected to ultracentrifugation at 235,000 × g for 45 min at 4°C to pellet the membranes. The resulting membrane pellet was resuspended using a homogenizer in buffer B (50 mM sodium phosphate, pH 7.4, 2 M NaCl) and ultracentrifuged again at 235,000 × g for 45 min at 4°C. This resuspension and ultracentrifugation cycle was repeated a total of three times to wash the membrane fraction. After washing, the membranes were resuspended using a homogenizer in buffer C (50 mM sodium phosphate, pH 7.4, 300 mM NaCl, 15% glycerol), and the membrane suspension was adjusted to a concentration of 200–250 mg/mL and stored at −80°C.

2.1.3 MexB solubilization

The membrane suspension (corresponding to at least 12 g of membranes, wet weight) was supplemented with dodecyl-β-D-maltoside (DDM) to a final concentration of 0.8% (w/v) and gently stirred at 4°C for 30 min to solubilize contaminating proteins. The mixture was then centrifuged using an SW 32 Ti rotor (Beckman Coulter) at 164,000 × g for 30 min at 4°C, and the resulting pellet was collected. The pellet was resuspended with a homogenizer and adjusted to final concentrations of 2% (w/v) DDM and 10 mM

imidazole. After stirring at 4°C for 1 h to solubilize MexB, the suspension was ultracentrifuged at 164,000 × g for 1 h at 4°C, and the supernatant was collected. When the total amount of membrane was less than 12 g, the membrane suspension was directly adjusted to 2% (w/v) DDM and 10 mM imidazole, stirred at 4°C for 1 h, and ultracentrifuged at 164,000 × g for 1 h at 4°C, after which the supernatant was collected.

2.1.4 Purification of MexB

Detergent DDM had previously been used for MexB purification; however, based on protocol optimization by a previous researcher, the procedure was modified to exchange DDM for CYMAL-7 during purification at the Ni–NTA step. This change was implemented to standardize detergent conditions and to avoid potential incompatibility among components—such as reduced complex stability or increased sample heterogeneity—when reconstituting the MexAB–OprM tripartite complex in vitro. Because OprM, the outer-membrane component of MexAB–OprM, is purified in CYMAL-7, switching MexB purification from DDM to CYMAL-7 facilitates detergent compatibility during complex reconstitution.

The solubilized supernatant was mixed with 5 mL of Ni-chelating Sepharose resin pre-equilibrated with buffer D (50 mM sodium phosphate, pH 7.4, 300 mM NaCl, 10 mM imidazole, 0.02% (w/v) CYMAL-7) and gently stirred at 4°C for 1 h. The resin slurry was then transferred to an open column, and the flow-through fraction was collected. The resin was washed with 50 mL buffer E (50 mM sodium phosphate, pH 7.4, 300 mM NaCl, 50 mM imidazole, 0.02% (w/v) CYMAL-7), and the wash fraction was collected. The resin was further washed with buffer F (50 mM sodium phosphate, pH 7.4, 300 mM NaCl, 150 mM imidazole, 0.02% (w/v) CYMAL-7). Bound MexB was eluted by

gently adding 15 mL buffer G (50 mM sodium phosphate, pH 7.4, 300 mM NaCl, 300 mM imidazole, 0.02% (w/v) CYMAL-7), and the eluate was collected. The pooled eluate was concentrated to 2.5 mL using a Spin-X UF 20 ultrafiltration device with a 100-kDa molecular weight cutoff (Corning).

The concentrated protein solution was loaded onto a Superdex 200 16/60 column (Cytiva) equilibrated with buffer H (20 mM sodium phosphate, pH 7.4, 150 mM NaCl, 0.02% (w/v) CYMAL-7), and the peak fractions were collected. These peak fractions were then loaded onto a Superdex 200 Increase 10/300 GL column (Cytiva) equilibrated with the same buffer for further purification. The final peak fractions were concentrated to 20 mg/mL and dialyzed against 20 mM sodium phosphate (pH 7.4) containing 0.02% (w/v) CYMAL-7 prior to crystallization.

2.1.5 Crystallization and cryoprotection of drug-free MexB

MexB crystals were grown at 4°C by the hanging-drop vapor-diffusion method.

For crystallization under mildly basic conditions, 1 μL of purified MexB (20 mg/mL) was mixed with 1 μL of reservoir solution containing 8–9% (w/v) polyethylene glycol (PEG) 4000, 0.1–0.2 M KCl, and 0.1 M HEPES (pH 8.0 or 8.5), and the drops were incubated at 4°C. For cryoprotection, crystals were transferred stepwise into reservoir solutions containing gradually increasing concentrations of glycerol. The glycerol concentration was initially 5% (v/v) and was increased in 5% (v/v) increments every 30 min to a final concentration of 25% (v/v). The crystals were then flash-cooled in liquid nitrogen.

For crystallization under mildly acidic conditions, 1 μL of MexB (20 mg/mL) was mixed with 1 μL of reservoir solution containing 7–8% (w/v) PEG 3350, 0.2 M $MgCl_2$

or 0.2 M $MgSO_4$ and 0.1 M 2-(N-morpholino) ethanesulfonic acid (MES), pH 6.5–6.8, and the drops were incubated at 4°C. For cryoprotection, the ethylene glycol concentration was increased from an initial 1% (v/v) in 2.5% (v/v) increments every 30 min to a final concentration of 25% (v/v). The crystals were then flash-cooled in liquid nitrogen.

These crystallization conditions were originally identified in our laboratory by Dr. R. Yonehara (unpublished data), and MexB was crystallized under these conditions with minor modifications.

2.1.6 X-ray Diffraction experiment and analysis

X-ray diffraction data for MexB crystals were collected on beamline BL44XU at SPring-8, Japan (24, 25), using an EIGER X 16M hybrid photon-counting pixel-array detector (Dectris). Diffraction images were processed with autoPROC (26) using XDS (27), and subsequent data processing was carried out with Phenix (28). Molecular replacement was performed with PHASER (29) using the DDM-bound MexB structure (PDB ID 3W9I) (21) as a search model. Model building was carried out with Coot (30), and structure refinement was performed with phenix.refine (31). Polder maps were generated with phenix.polder (32). Structural superpositions were performed with SUPERPOSE in the CCP4 program suite (33). Figures were prepared with PyMOL (Schrödinger). Diffraction data for MexB previously collected by other researchers in my laborarory were acquired using an MX300-HE detector (Rayonix), and the diffraction images were processed with HKL-2000 (34). Subsequent data processing and structure refinement were performed as described above.

2.2 Result

2.2.1 Purification of MexB

During the first size-exclusion chromatography step, MexB eluted as multiple peaks (Fig. 2.2.1.1), suggesting that the protein existed in oligomeric forms in solution. Therefore, fractions corresponding to an elution volume of 50–60 mL were pooled, concentrated, and subjected to a second size-exclusion chromatography step. In this run, the purified MexB protein eluted as a single peak (Fig. 2.2.1.2), and its purity was confirmed by SDS–PAGE, which showed a single homogeneous band (Fig. 2.2.1.3).

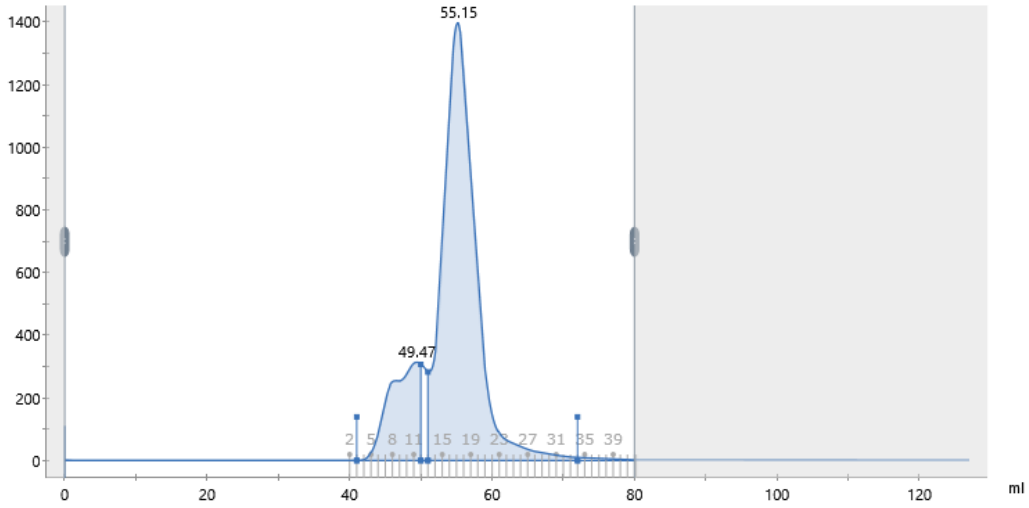

Figure 2.2.1.1. The elution profile from gel filtration column of MexB.
SEC chart MexB on a Superdex 200 16/60 column column with buffer H.

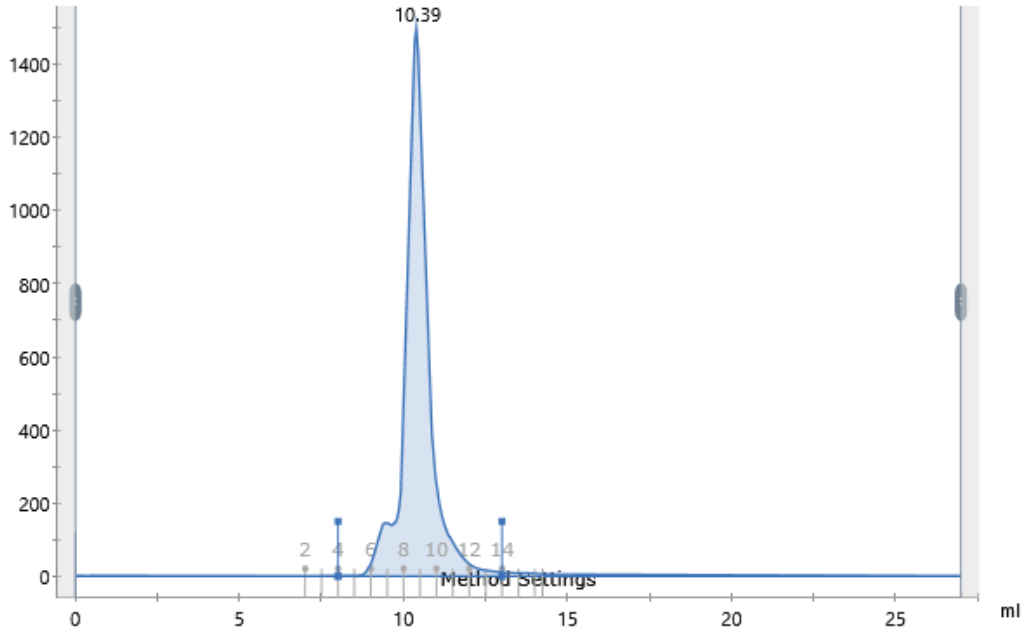

Figure 2.2.1.2. The elution profile from gel filtration column (Superdex 200 Increase 10/300 GL column) of MexB.

The peak fractions from the Superdex 200 16/60 column were collected and further purified on a Superdex 200 Increase 10/300 GL column.

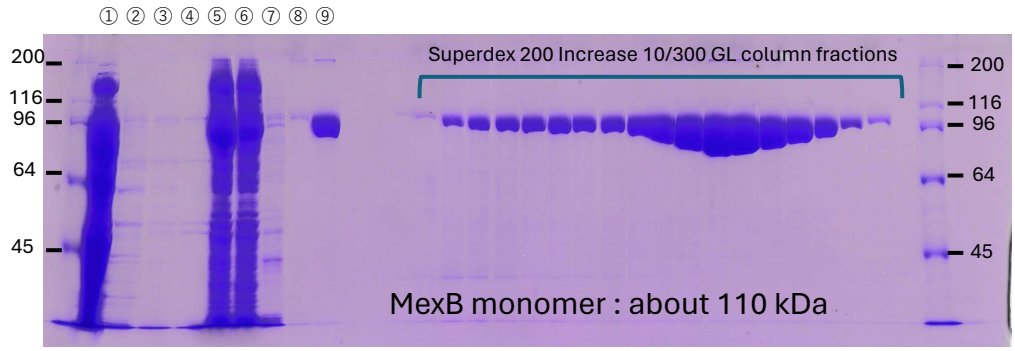

Figure 2.2.1.3. SDS-PAGE of MexB.

①Supernatant from disruption, ②-④ Membrane wash fractions, ⑤ Solubilized supernatant, ⑥ Ni-NTA flow-through, ⑦ Ni-NTA wash 1, ⑧ Ni-NTA wash 2, ⑨ Ni-NTA elution

2.2.2 Crystallization

Under mildly basic conditions, MexB crystals appeared within a few days and grew to a size suitable for diffraction within approximately one week (Fig. 2.2.2A). In contrast, under mildly acidic conditions, MexB crystals took approximately 1–2 weeks to appear (Fig. 2.2.2.B).

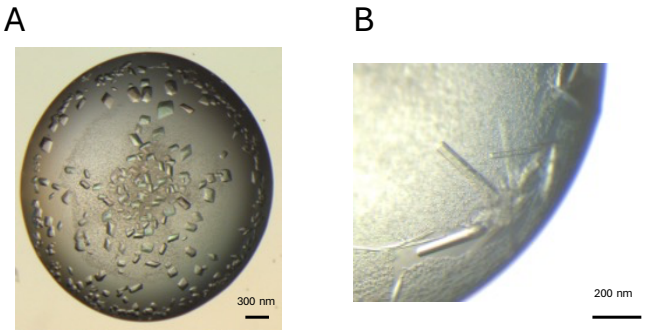

Figure 2.2.2. Crystals of drug-free MexB

(A) Crystals of mildly basic conditions MexB

(B) Crystals of mildly acidic conditions MexB

2.3.3 Structure determination

Diffraction data from MexB crystals grown under crystallization conditions containing 0.1 M HEPES pH 8.5, 0.1 M KCl, and 8% (w/v) PEG 4000 were collected to 3.00 Å resolution. These crystals belonged to space group *C*2, with unit-cell parameters a = 204.06, b = 169.99, c = 171.97 Å, and $\alpha = \gamma = 90°$, $\beta = 101.51°$.

Diffraction data from crystals grown under conditions containing 0.1 M MES pH 6.5, 0.2 M $MgSO_4$, and 9% (w/v) PEG 3350 were obtained to 2.44 Å resolution. These crystals belonged to space group $P2_12_12_1$, with unit-cell parameters a = 130.79, b = 156.10, c = 256.07 Å, and $\alpha = \beta = \gamma = 90°$. Data collection statistics are summarized in Table 2.2.3.

A previously collected MexB dataset obtained from crystals grown under the mildly basic crystallization condition had a resolution of 2.30 Å resolution, which was higher than that of the mildly basic MexB crystals collected in this study. Therefore, the 2.30 Å resolution dataset was used for structure determination of MexB under the mildly basic condition. In contrast, for MexB crystals grown under the mildly acidic crystallization condition, we were unable to determine any substrate-bound MexB structures, as described in Chapter 3, and thus no structure determination was carried out for the mildly acidic MexB crystals.

Table 2.2.3. Data collection statistics and refinement of MexB.

	MexB	MexB	MexB
pH	8.5	6.5	8
Measurement date	3/7/2024	6/11/2023	13/11/2017
Ditector	EIGER X 16M	EIGER X 16M	MX300-HE
Data collection			
Wavelength (Å)	0.90	0.90	0.90
Space group	*C* 2	$P2_12_12_1$	*C* 2
Unit cell			
a, b, c (Å)	204.06, 169.99, 171.97	130.79, 156.10, 256.07	207, 168.9 172.2
α , β , γ (°)	90, 101.51, 90	90, 90, 90	90, 102.23, 90
Resolution (Å)	168.51-3.00 (3.05-3.00)	133.29-2.44 (2.48-2.44)	40.55-2.30 (2.34-2.30)
Unique reflections	114532	194476	251734
R_{merge}	0.14 (3.77)	0.09 (2.83)	0.080 (>1.0)
CC1/2	0.99 (0.354)	0.99 (0.32)	0.999 (0.406)
Completeness (%)	100 (100)	100 (100)	99.5 (100)
I/σ (I)	7.6 (0.5)	10.2 (0.8)	24.1(1.0)
Redundancy	6.9(6.6)	6.6 (6.8)	4.0 (4.0)
Refinement			
Resolution (Å)			40.55-2.30
R_{work} / R_{free}			0.2204/0.2552
R.m.s.d. from ideal geometry			
Bond lengths (Å)			0.008
Bond angles (°)			0.99
Ramachandran plot			
Favored (%)			97.89
Allowed (%)			2.11
Outliers (%)			0.00

Values in the parentheses are for the highest resolution shells.

2.2.4 Overall structure of MexB in mildly basic condition.

We crystallized MexB under mildly basic condition, yielding a structure in space group C2 at 2.30 Å resolution. The crystallographic asymmetric unit contained one MexB homotrimer. The MexB comprises 1,055 residues, of which at least 1,024 residues were modeled (Fig. 2.2.4.1 A).

Each subunit consists of a TM domain with 12 helices, a porter domain harboring the substrate-binding pockets, and a funnel-like domain. The three protomers are asymmetric and adopt distinct conformations (Fig. 2.2.4.1B, C). The centroid-to-centroid distances between a porter domain subdomains PN1 and PN2 were 26.5, 28.3, and 29.8 Å for chains A, B, and C, respectively, and those between a porter domain subdomains PC1 and PC2 were 25.9, 28.8, and 24.1 Å (Table 2.2.4.1). Distances among residues involved in proton translocation (MexB D407 and D408 in TM4, K939 in TM10, and T976 in TM11) further distinguished the protomers: in chains A and B, K939–D408 measured 2.66 and 2.68 Å, whereas in chain C, K939–T976 was 2.87 Å (Fig. 2.2.4.1C, Table 2.2.4.1). Based on these metrics, we assigned chains A, B, and C to the Access, Binding, and Extrusion states, respectively. The pairwise Ca Root Mean Square Deviations (RMSDs) between our three protomers were 2.34 Å (Access–Binding), 2.59 Å (Access–Extrusion), and 3.34 Å (Binding–Extrusion) (Table 2.2.4.2). Superposition with previously reported MexB structures (21) in the Access, Binding, and Extrusion states gave Ca RMSDs of 0.96 (0.95), 0.66 (0.70), and 0.74 (0.72) Å (Fig. 2.2.4.2.A, Table 2.2.4.3), respectively, indicating overall similarity; the Access state showed a slight deviation. In the Access protomer, part of the PC2 Ca4 segment (L843–W858) together with part of PC2 Ca3 (K701–Q708) tilted toward PC1, while a part of the PC1 Ca2 segment (K649–M662) shifted outward, away from PC2 (Figure

2.2.4.2A, B). Crystal contacts with a symmetry mate were observed around Ca3, potentially imposing local steric constraints, whereas no symmetry contacts were detected around Ca2 or Ca4. The TM4/TM5 and TM10/TM11 helices likewise exhibited conformational changes. In prior structures (21), TM4, TM5, and TM10 contacted symmetry mates; accordingly, differences in crystal packing likely contribute to the variation in TM-domain Ca RMSDs (Figure 2.2.4.3A, B). These domain rearrangements likely account for the elevated Ca RMSD observed for the Access state relative to the reference structure (PDB ID 3W9I).

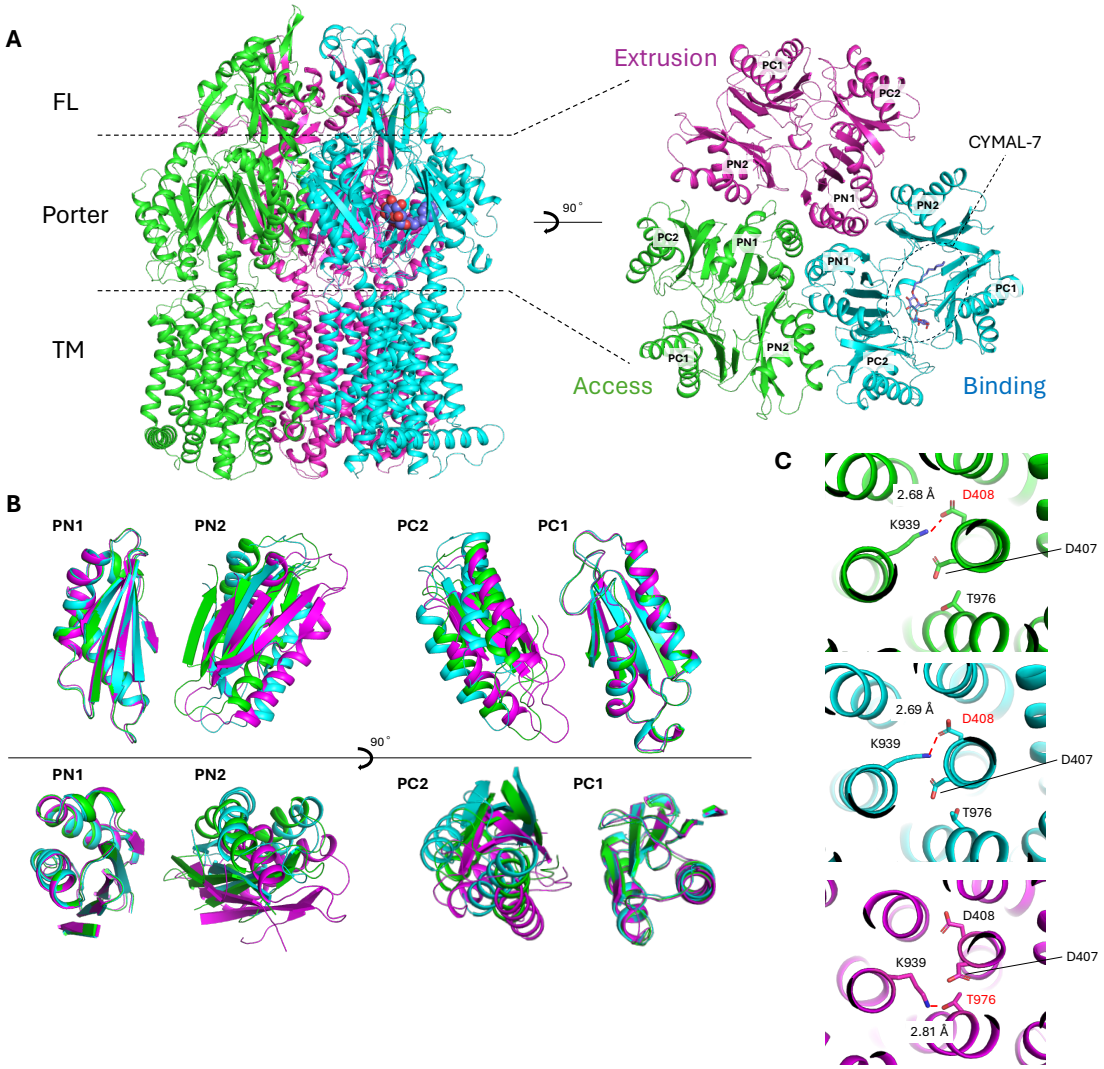

Figure 2.2.4.1 Structure of drug-free MexB obtained under mildly basic conditions.

(A) Overall structure of the drug-free MexB trimer (left) and top view of the porter domain (right). CYMAL-7 is depicted as spheres or sticks. (B) Superposition of the porter domains from the three protomers. Superposition was performed using PN1- or PC1-based superpositions. Subdomains are defined as PN1 (40–130, 814–818), PN2 (136–180, 284–328), PC1 (571–666), and PC2 (679–717, 821–858). (C) Comparison of residues implicated in proton translocation across protomers. Side chains of D407, D408, K939, and T976 are shown as sticks. Hydrogen bonds are shown as red dashed lines.

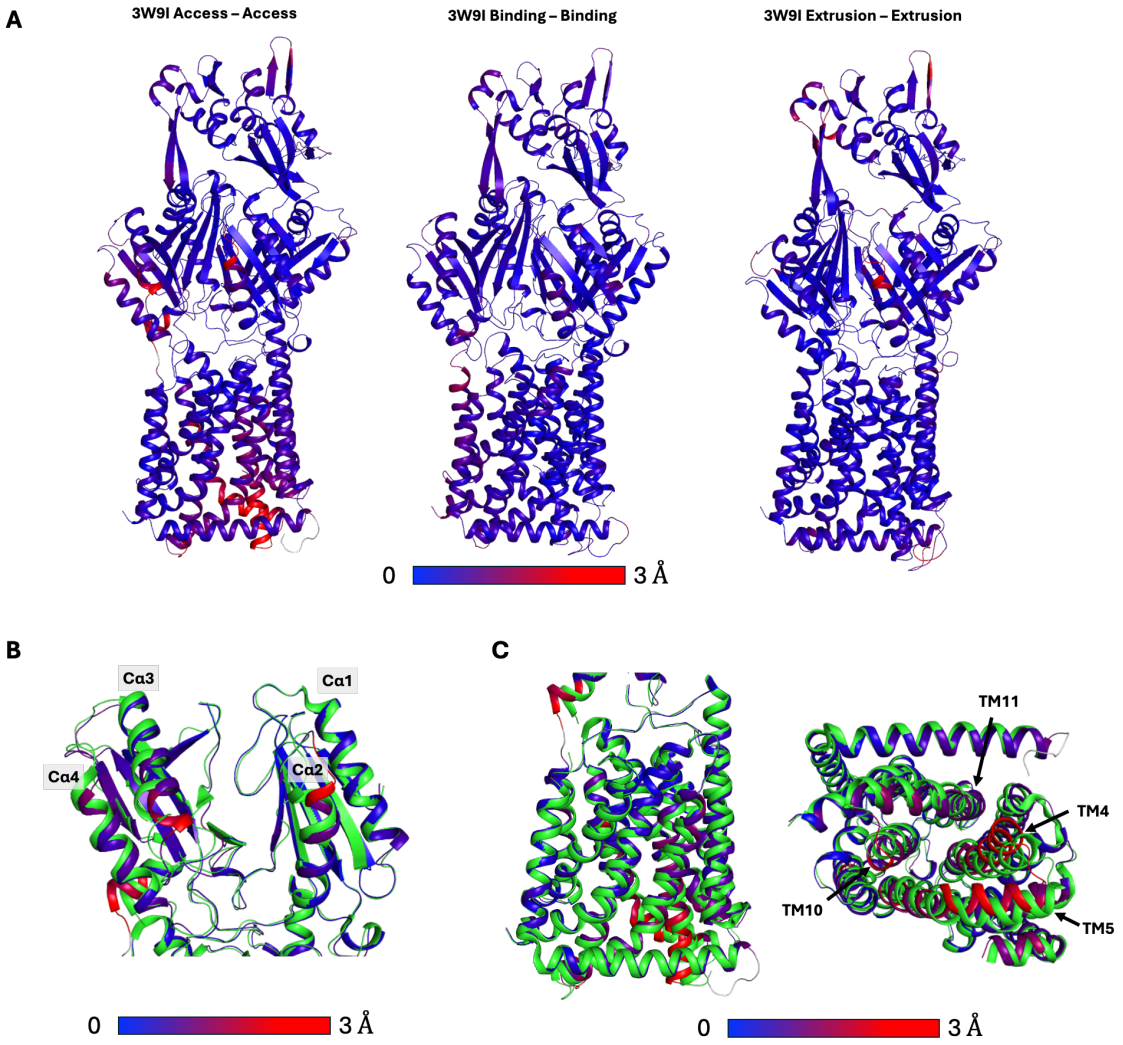

Figure 2.2.4.2. Structural comparison of MexB for each protomer with the previous structure.

(A) Drug-free MexB model shown in ribbon representation, with per-residue Cα RMSD values mapped onto the structure after superposition onto MexB (PDB ID 3W9I). (B) Superposition of the porter domains of the Access protomers. The previously reported MexB structure (PDB ID 3W9I) is shown in green. In our structure, the PC2 Cα3 and Cα4 segments tilt toward the PC1 side, whereas the PC1 Cα2 segment flares outward. (C) Superposition of the transmembrane (TM) domains of the Access protomers. The previously reported MexB structure (PDB ID 3W9I) is shown in green.

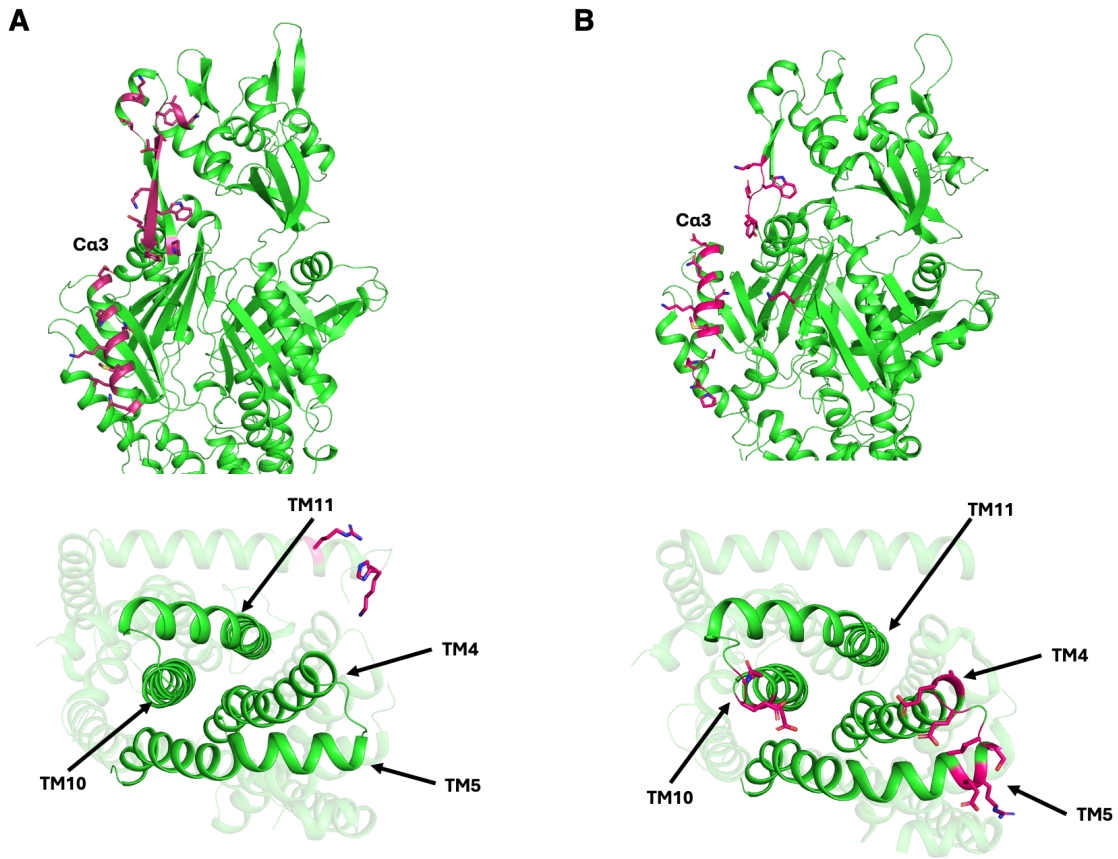

Figure 2.2.4.3. Amino acid residues involved in contact with symmetric molecules.

(A) Amino acid residues (pink, stick representation) contacting symmetry molecules in the Access protomer of MexB crystallized under mildly basic conditions. (B) Amino acid residues (pink, stick representation) contacting symmetry molecules in the Access protomer of MexB in the previously reported structure (PDB ID 3W9I).

Table 2.2.4.1. Center-of-mass distances between subdomains within the porter domain and distances between residues involved in proton transfer in each chain.

	Distance (Å)			
	PN1-PN2 [a]	**PC1-PC2** [b]	**D408-K939**	**K939-T976**
Chain A	26.5	26.2	2.68	8.41
Chain B	28.3	29.1	2.69	6.78
Chain C	29.8	24.5	9.04	2.81

[a] PN1 (40–130 and 814–818), and PN2 (136–180 and 284–328)

[b] PC1 (278–281 and 571–666), and PC2 (679–717 and 821–858)

Table 2.2.4.2 Cα atom RMSD of Drug-free MexB each protomer.

	Chain A	Chain B	Chain C
Chain A		2.34	2.59
Chain B			3.34
Chain C			

The Cα RMSD values (Å) for residues 1–1025 in each protomer were calculated using the program SUPERPOSE in the CCP4 suite.

Table 2.2.4.3. Cα atom RMSD of each protomer relative to reported MexB.

		MexB (PDB ID 3W9I)					
		Chain A	**Chain B**	**Chain C**	**Chain D**	**Chain E**	**Chain F**
Drug-freeMexB	**Chain A**	0.96	2.43	3.32	0.95	2.46	2.65
	Chain B	2.60	0.66	3.32	2.70	0.70	3.37
	Chain C	2.85	3.32	0.74	2.76	3.37	0.72

The Cα RMSD values (Å) for residues 1–1025 in each chain were calculated using the program SUPERPOSE in the CCP4 suite.

2.2.5 Binding mode of CYMAL-7

In the Binding protomer, CYMAL-7 was located at the entrance between the PC1 and PC2 subdomains (Fig. 2.2.5.1A, B). Its maltoside headgroup was stabilized by hydrophobic contacts with F617, F666, and P669 and by hydrogen bonds to R716 and Q718. The hydrophobic moiety primarily contacted residues in PC1 (K134, F573, F610, F628, and M630) as well as F672 in the PN1–PN2 connecting loop and was oriented toward the distal binding pocket (DBP) (Fig. 2.2.5.1B). Thus, CYMAL-7 occupies an intermediate site between the proximal and distal binding pockets, distinct from the binding positions reported for DDM and LMNG (Fig 2.2.5.2). In addition to the density for CYMAL-7 at the PC1–PC2 entrance, we also observed weak positive difference density within the DBP. This density was not sufficiently clear to assign a ligand unambiguously and could arise from crystallization components; accordingly, we did not model any ligand in this site.

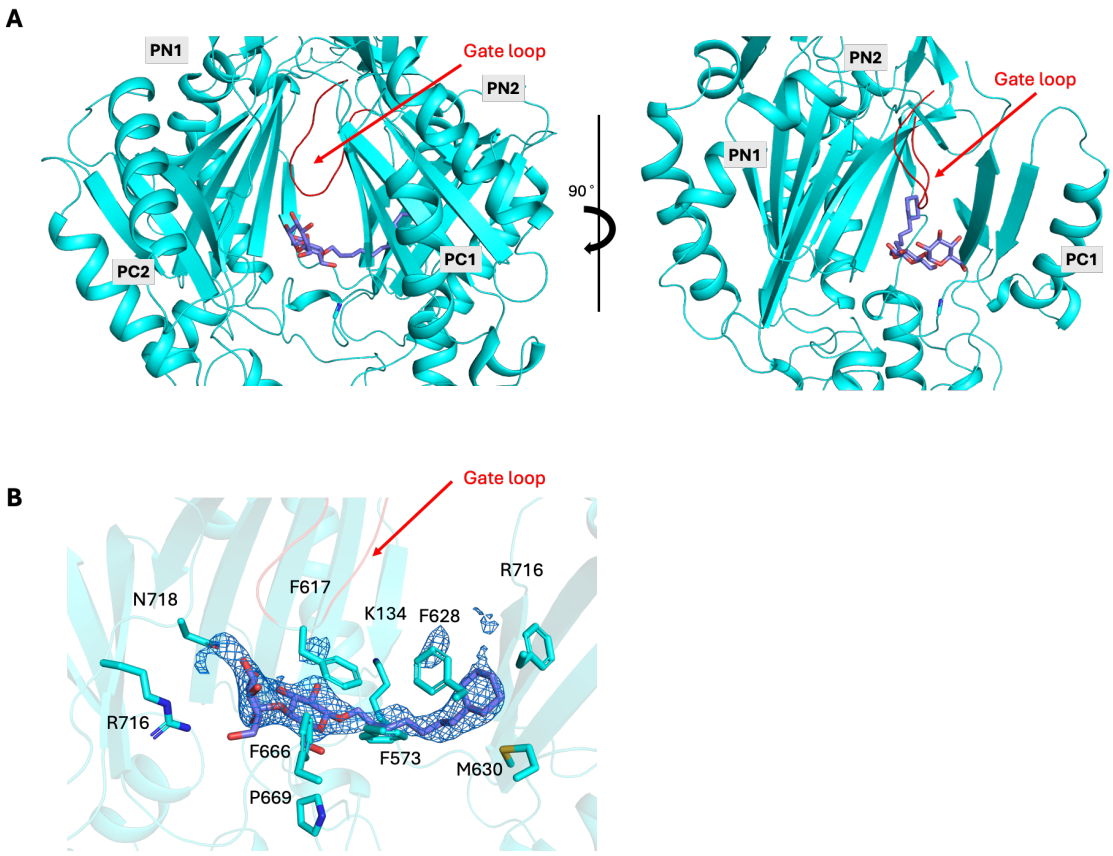

Figure 2.2.5.1. CYMAL-7 bound to the substrate-binding pocket.

(A) Left: Binding protomer viewed from the cytoplasmic side, showing CYMAL-7 positioned adjacent to the gate loop. Right: the same view rotated by 90°. The foreground PC2 subdomain is hidden to better visualize the binding pocket. The gate loop is colored red. **(B)** Close-up of the CYMAL-7 binding mode. Residues contacting CYMAL-7 are shown as sticks. The Polder map for CYMAL-7 is contoured at 3.0σ and shown as a blue mesh.

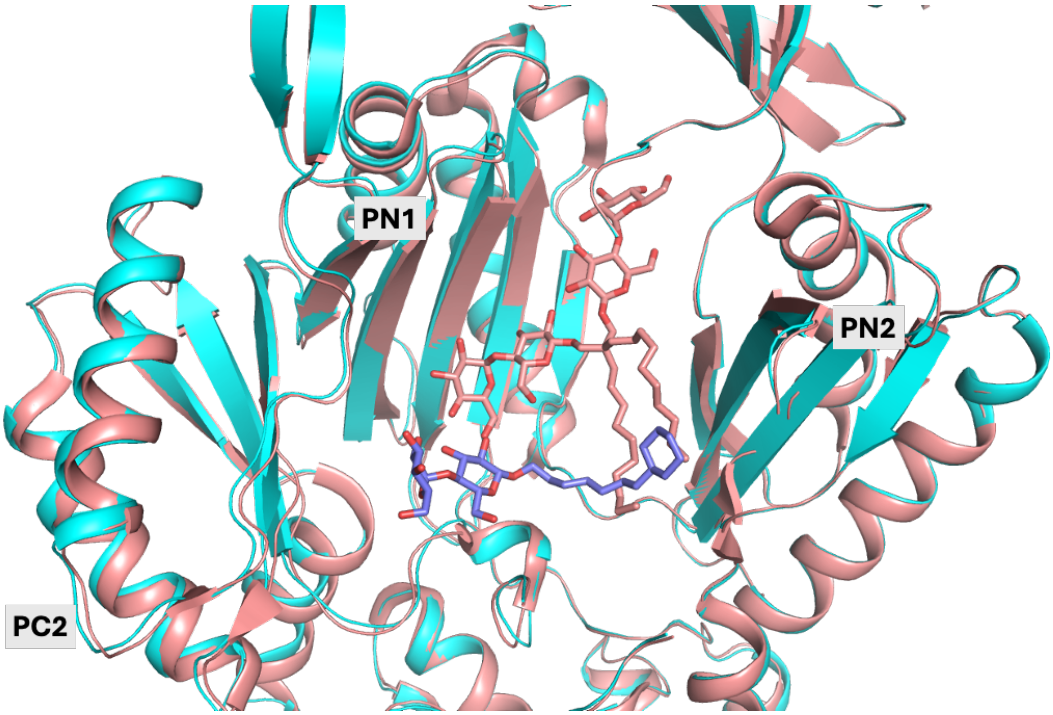

Figure 2.2.5.2 Differences in binding positions between CYMAL-7 and LMNG.

Structural comparison of drug-free MexB (cyan) with LMNG-bound MexB (PDB ID 6IIA, salmon), superposed by least-squares fitting of the Cα atoms of residues 1–1030. The foreground PC1 subdomain is hidden to better visualize the detergent-binding site.

3. The structure of antibiotics-bound MexB

In Chapter 3, we performed substrate soaking experiments on MexB crystals grown under both mildly basic and mildly acidic crystallization conditions. A panel of known MexB substrates—including levofloxacin, chloramphenicol, carbenicillin, erythromycin, ampicillin, rifampicin, rhodamine 6G, cefotaxime, tetracycline, doxorubicin, and cefpirome—was soaked into MexB crystals, and X-ray diffraction data were collected.

Among these complexes, clear electron density corresponding to chloramphenicol was observed in the distal binding pocket (DBP) only for chloramphenicol-soaked MexB. The chloramphenicol-bound MexB structure forms a homotrimer, in which the three protomers adopt the Access, Binding, and Extrusion conformations, as observed for the CYMAL-7–bound MexB structure. Structural analysis of this complex enabled us to identify amino acid residues in the DBP that are critical for chloramphenicol binding.

3.1 Material and Methods

3.1.1 Procedures From transformation to MexB crystallization

The procedures from transformation to MexB crystallization were carried out as described in Section 2.1.

3.1.2 Drug soaking of MexB crystals and cryoprotection

For crystals grown under mildly basic conditions, MexB crystals that had reached a suitable size were transferred to 50 μL of reservoir solution containing 8–9% (w/v) PEG 4000, 0.1–0.2 M KCl, and 0.1 M HEPES (pH 8.0 or 8.5) and were allowed to equilibrate for 12 h. The crystals were then transferred to the same reservoir solution supplemented with substrate and soaked for at least 24 h. For cryoprotection with glycerol, crystals were transferred stepwise into reservoir solutions in which the glycerol concentration was increased from an initial 1% (v/v) to 5% (v/v) in 1% (v/v) increments every 15 min and then further increased to a final concentration of 25% (v/v). The crystals were then flash-cooled in liquid nitrogen.

For crystals grown under mildly acidic conditions, MexB crystals that had reached a suitable size were transferred to 50 μL of reservoir solution containing 7–8% (w/v) PEG 3350, 0.2 M $MgCl_2$ or 0.2 M $MgSO_4$, and 0.1 M MES (pH 6.5–6.8) and were allowed to equilibrate for 12 h. The crystals were then transferred to the same reservoir solution supplemented with substrate and soaked for at least 24 h. For cryoprotection with ethylene glycol, crystals were transferred stepwise into reservoir solutions in which the ethylene glycol concentration was increased from an initial 1% (v/v) to 5% (v/v) in 1% (v/v) increments every 15 min and then further increased to a final concentration of 25% (v/v). The crystals were then flash-cooled in liquid nitrogen.

Substrates used for soaking were selected from compounds previously reported to be exported by MexB, including the antibiotics levofloxacin, chloramphenicol, carbenicillin, erythromycin, ampicillin, rifampicin, cefotaxime, cefpirome, and tetracycline, the fluorescent dye rhodamine 6G, and the anticancer drug doxorubicin.

3.1.3 X-ray Diffraction experiment and analysis

X-ray diffraction data for substrate-bound MexB crystals were collected on beamline BL44XU at SPring-8 (35, 36) using an EIGER X 16M hybrid photon-counting pixel-array detector (Dectris). Diffraction images were processed with autoPROC (26) using XDS (27), and subsequent data processing was performed with Phenix (28). Molecular replacement was carried out with PHASER (29) using the corresponding drug-free MexB structure as the search model. Model building was performed with Coot (30), and structure refinement was carried out with phenix.refine (31).

3.2 Result

3.2.1 Substrate soaking and structure determination in mildly basic conditions.

X-ray diffraction data were successfully collected for MexB crystals soaked with rhodamine 6G, chloramphenicol, erythromycin, ampicillin, carbenicillin, cefotaxime, tetracycline, doxorubicin, cefpirome, and cloxacillin. Soaking with these substrates did not change the space group (*C*2), and no substantial differences in the unit-cell parameters were observed compared with the drug-free crystals. Statistics for data collection and processing are summarized below (Table 3.2.1).

Table 3.2.1 Data collection statistics of substrate-bound MexB under mildly basic conditions.

Substrate	Rhodamine	Chloramphenicol	Erythromycin	Ampicillin	Carbenicillin	Cefotaxime	Tetracycline	Doxorubicin	Cefpirome	Cloxacillin
cryoprotectant	25% Glycerol									
Wave length (Å)	0.9									
a	204.7	204.87	205.73	205.3	204.41	204.37	204.08	205.3	204.87	203.4
b (Å)	169.2	169.17	168.7	169.18	168.91	169.24	170.25	170.02	169.49	169.68
c	171.8	171.92	172.28	171.9	171.88	171.76	172.06	172.28	171.74	172.17
β (◦)	101.8	102.15	101.95	102.06	101.82	101.7	101.55	101.75	101.87	101.69
Resolution range (Å)	168.1– 2.60	129.2–2.89	129.29–2.65	129.37– 2.86	129.06–2.75	129.22–2.87	129.62–3.39	129.81–3.12	129.43–3.00	129.16–3.09
	(2.64–2.60)	(2.93–2.89)	(2.70–2.65)	(2.90–2.86)	(2.80–2.75)	(2.92–2.87)	(3.45–3.39)	(3.17–3.12)	(3.05–3.00)	(3.15–3.09)
R_{merge}	0.044(5.443)	0.111 (3.92)	0.096 (4.20)	0.123(3.79)	0.101(2.916)	0.117(3.981)	0.194(4.308)	0.102(3.25)	0.138(4.036)	0.083(5.362)
CC1/2	0.996(0.387)	0.991(0.353)	0.996(0.330)	0.989 (0.388)	0.990(0.365)	0.997(0.386)	0.992(0.35)	0.993(0.349)	0.996(0.316)	0.997(0.395)
Unique Reflections	175,419	128,001	165,236	132,401	147,381	129,461	79,427	102,813	114,354	103,943
<I> / < σ_I>	10.0(0.5)	10.3 (0.6)	8.8 (0.4)	9.1(0.7)	8.6 (0.6)	9.1 (0.5)	5.9 (0.7)	10.6 (0.7)	8.9 (0.6)	9.2(0.3)
Completeness (%)	100 (100)	100 (100)	100 (100)	100 (100)	100 (100)	100 (100)	100 (100)	100 (100)	100 (100)	100 (100)
Redundancy	7.2(7.2)	7.4 (6.8)	6.3 (6.4)	6.9 (6.5)	5.2(5.2)	7.4 (6.9)	7.4(6.6)	7.3 (7.5)	7.4(7.0)	7.5(7.7)

3.2.1 Substrate soaking and structure determination in mildly acidic conditions.

X-ray diffraction data were successfully collected for MexB crystals soaked with rhodamine 6G, erythromycin, ampicillin, carbenicillin, cefotaxime, tetracycline. Soaking with these substrates did not alter the space group ($P2_12_12_1$), and no substantial changes in the unit-cell parameters were observed compared with the drug-free crystals. Data collection and processing statistics are summarized below (Table 3.2.2).

Table 3.2.2 Data collection statistics of substrate-bound MexB under mildly acidic conditions.

substrate	Rhodamine	Eryhromycin	Ampicillin	Cefotaxime	carbenicillin	tetracycline
cryoprotectant	25% Ethylene glycol					
Wave length (Å)	0.9					
a	131.03	131.16	130.48	130.44	131.28	130.74
b (Å)	156.87	156.98	157.05	157.18	157.38	157.22
c	259.72	258.6	258.82	259.98	260.11	260.38
α, β, γ (°)	90	90	90	90	90	90
Resolution range (Å)	168.1– 2.60	129.29–2.65	129.37– 2.86	129.22–2.87	134.65-2.95	116.84-3.80
	(2.64–2.60)	(2.70–2.65)	(2.90–2.86)	(2.92–2.87)	(3.00-2.95)	(3.87-3.80)
R_{merge}	0.044(5.443)	0.096 (4.20)	0.123(3.79)	0.117(3.981)	0.278(4.043)	0.311(7.690)
CC1/2	0.996(0.387)	0.996(0.330)	0.989 (0.388)	0.997(0.386)	0.996(0.349)	0.996(0.794)
Unique Reflections	175,419	165,236	132,401	129,461	114265	53530
$\langle I \rangle / \langle s_I \rangle$	10.0(0.5)	8.8 (0.4)	9.1(0.7)	9.1 (0.5)	8.2(0.7)	6.7(0.4)
Completeness (%)	100 (100)	100 (100)	100 (100)	100 (100)	100 (100)	100 (100)
Redundancy	7.2(7.2)	6.3 (6.4)	6.9 (6.5)	7.4 (6.9)	7.4 (7.6)	7.3(7.6)

3.2.2 Structure of Antibiotics-bound MexB

Various drugs were soaked into MexB crystals grown under both mildly basic and mildly acidic crystallization conditions. However, a chloramphenicol-bound MexB structure could be determined only from crystals obtained under the mildly basic conditions. For all soaked crystals grown under the mildly acidic conditions, no interpretable electron density corresponding to the substrates was observed. We therefore report here only the structure of chloramphenicol-bound MexB obtained under the mildly basic crystallization conditions. The structural analysis statistics are shown Table 3.2.2.

Table 3.2.2 Refinement of Chloramphenicol-bound MexB

	Chloramphenicol-bound MexB
Refinement	
Resolution (Å)	51.02-2.89
R_{work} / R_{free}	0.2237/0.2798
R.m.s.d. from ideal geometry	
Bond lengths (Å)	0.009
Bond angles (°)	1.17
Ramachandran plot	
Favored (%)	92.39
Allowed (%)	7.57
Outliers (%)	0.03

3.2.3 Overall structure of Chloramphenicol-bound MexB

We determined the X-ray crystal structure of MexB in complex with chloramphenicol (Chl) at 2.89 Å resolution. Chl-MexB forms an asymmetric trimer, with protomers adopting the access, binding, and extrusion states (Fig. 3.2.3.1A). Relative to drug-free MexB (space group *C*2 MexB) structure, the Ca RMSDs for the Access, Binding, and Extrusion protomers were 0.41 Å, 0.62 Å, and 0.46 Å, respectively (Table 3.2.3.1).
A single Chl molecule was observed in the DBP of the Binding protomer, whereas no Chl density was detected in the Access or Extrusion protomers (Fig. 3.2.3.1A, B). Chl occupied the DBP groove, with no binding observed in the DBP cave or the proximal binding pocket (PBP). Only 6 residues lay within 3.5 Å of the ligand—Q125, R128, F178, G179, S180, and Q273—comprising polar side chains (Q125, R128, S180 and Q273) together with hydrophobic-trap residues (F178, G179) (Fig. 3.2.3.1.B).
In AcrB–substrate complexes, doxycycline (*37*) and minocycline (*38*) bind in the DBP groove in a manner like chloramphenicol (Fig. 3.2.3.2A, B). In the doxycycline complex, F178 and F615 sandwich the aromatic rings of the antibiotic, while N274 provides polar contacts, thereby anchoring the drug in the DBP groove. Minocycline binds at essentially the same position as doxycycline and adopts a very similar pose. By contrast, the aromatic ring of Chl is separated from F178, F615 by >10 Å, and no π–π interaction is not observed in Chl-MexB (Fig. 3.2.3.1B). Chl also approaches Q125 near the exit gate of the Binding protomer, locating deeper within the DBP groove than previously reported drug-binding sites in AcrB (Fig. 3.2.3.2A, B, C).

In MexB, the detergents DDM and LMNG (11, 21, 22) and the inhibitor ABI-PP (*21*) occupy the DBP (Fig. 3.2.3.3A, B, C, D). In those structures, DDM adopts two binding

modes: (i) contacting V47, S48, L117, Q125, R128, K151, F178, G179, Q273, D274, I277, and F628 (PDB ID 3W9I) (16); and (ii) contacting V47, S48, Q125, G179, S180, Q273, F615, N616, and F617 (PDB ID 2V50) (7). The union of DDM contacts therefore includes V47, S48, L117, Q125, R128, K151, F178, G179, S180, Q273, D274, I277, F615, N616, F617, and F628, of which Q125, R128, F178, G179, S180, and Q273 are also engaged by Chl (Fig. 3.2.3.3C, D).

LMNG, owing to its larger size, makes extensive contacts across the DBP; residues that overlap with Chl are R128, F178, G179, S180, and Q273, whereas Q125 is not implicated in reported LMNG complexes (Fig. 3.2.3.3B). ABI-PP strongly interacts with F178 and binds at a position slightly offset from those of LMNG and DDM. Consequently, residues common to Chl and ABI-PP are limited to R128, F178, and S180, whereas Q125, G179, and Q273 are not shared (Fig. 3.2.3.3A).

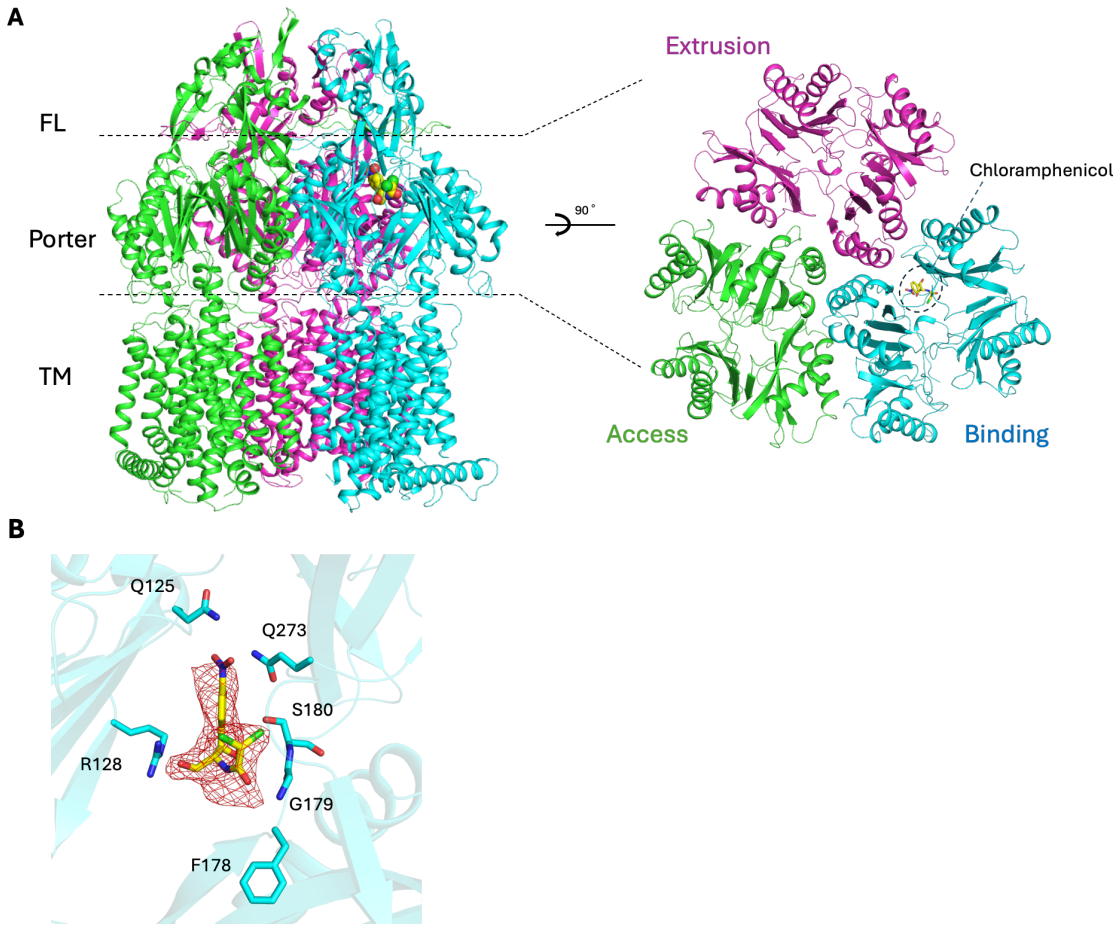

Fig. 3.2.3.1 Structure of the chloramphenicol-bound MexB.

(A) Overall structure of the chloramphenicol-bound MexB trimer (left) and top view of the porter domain (right). Chloramphenicol is shown as spheres in the left panel and as sticks in the right panel. The Access, Binding, and Extrusion protomers are colored green, cyan, and magenta, respectively.

(B) Close-up view of the chloramphenicol-binding site. The bound chloramphenicol molecule is shown as yellow sticks, and contacting residues are shown as sticks. The polder map for chloramphenicol is contoured at 3.0 σ and shown as a red mesh.

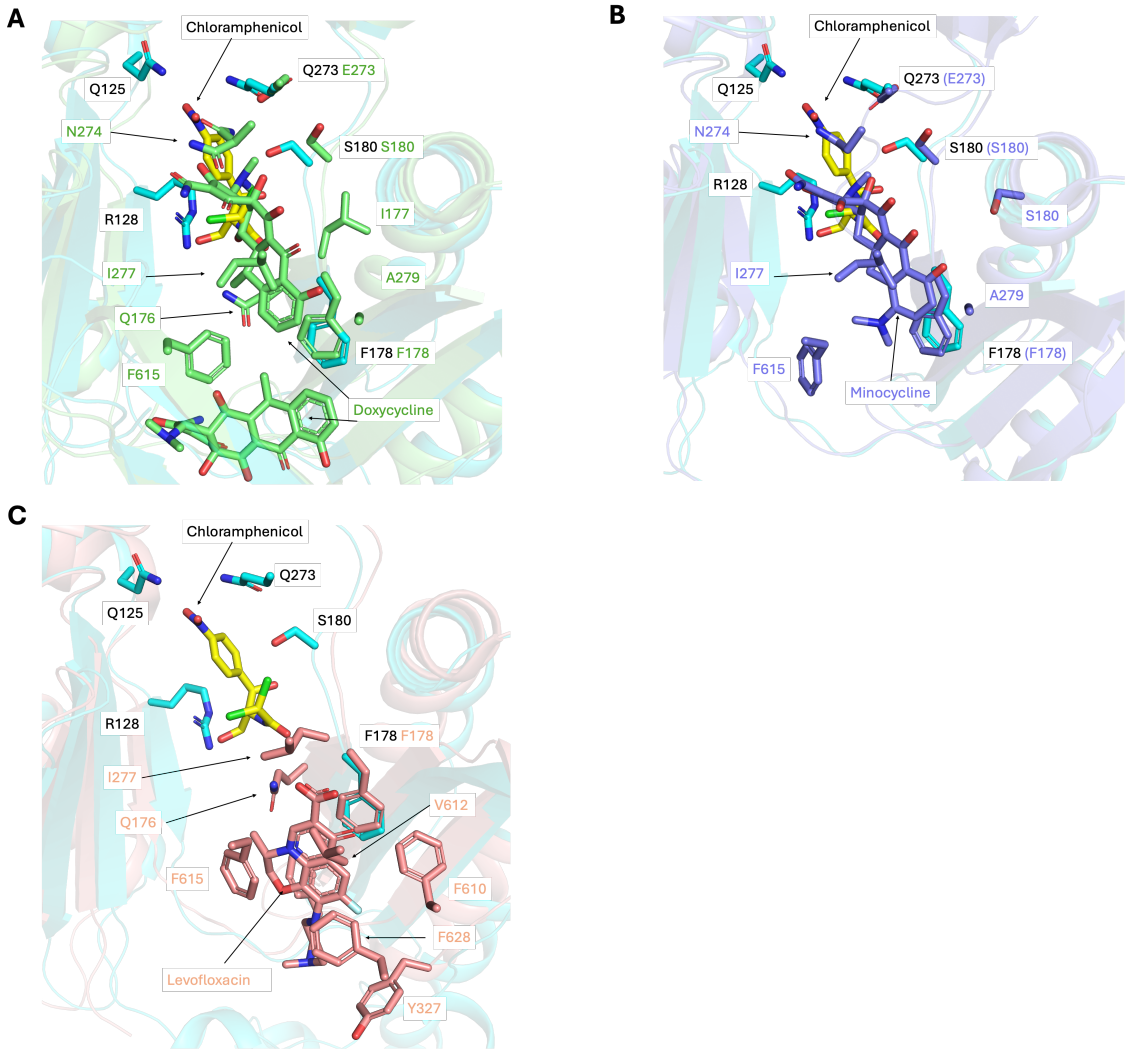

Fig.3.2.3.2. Superposition of the chloramphenicol-bound MexB with drug-bound AcrB structures.

(A) Superposition of doxycycline-bound AcrB (PDB ID 7B8R) with chloramphenicol-bound MexB. MexB residues are shown in cyan; AcrB residues are light green.

(B) Superposition of minocycline-bound AcrB (PDB ID 4DX5) with chloramphenicol-bound MexB. MexB residues are shown in cyan; AcrB residues are purple blue.

(C) Superposition of levofloxacin-bound AcrB (PDB ID 7B8T) with chloramphenicol-bound MexB. MexB residues are shown in cyan; AcrB residues are pink.

Corresponding AcrB residues are indicated by colored numbers.

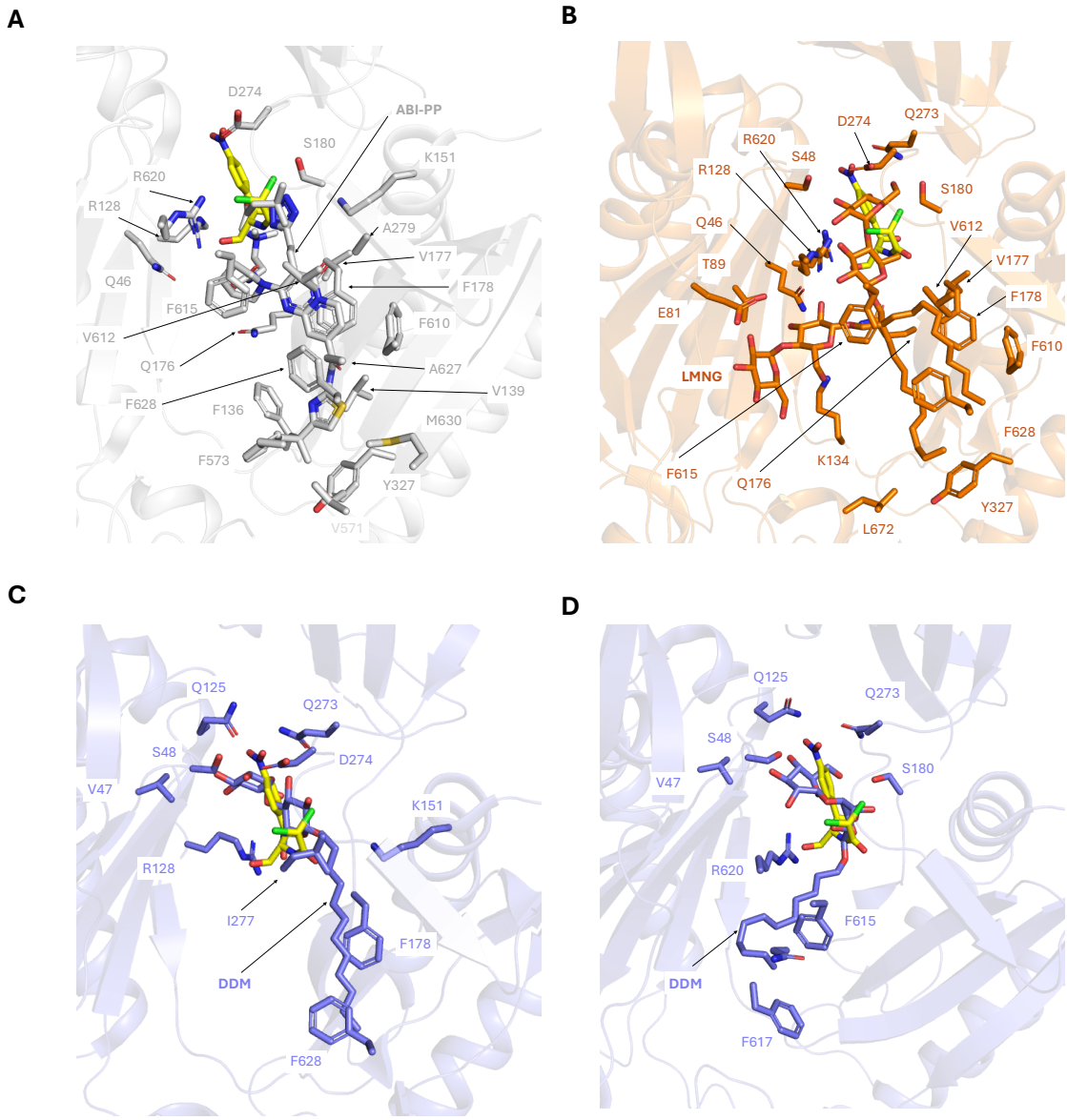

Fig.3.2.3.3. Structural comparison of chloramphenicol-bound MexB with previously reported MexB structures.

(A) Superposition of chloramphenicol-bound MexB with ABI-PP–bound MexB (PDB ID 3W9J).

(B) Superposition of chloramphenicol-bound MexB with LMNG-bound MexB (PDB ID 6IIA).

(C) Superposition of chloramphenicol-bound MexB with DDM-bound MexB (PDB ID 3W9I).

(D) Superposition of chloramphenicol-bound MexB with DDM-bound MexB (PDB ID 2V50).

4. In vitro drug resistance assay of cells harboring deep binding pocket variants.

In Chapter 4, to validate the contribution of distal binding pocket (DBP) residues identified from the chloramphenicol-bound MexB structure, we generated single-substitution MexB variants (Q125E, R128E, F178Y, F178W, F178A, G179A, S180A, and Q273E) and evaluated their susceptibility to chloramphenicol (Chl).

An inactive efflux pump control (ΔmexB), wild-type MexB, and each single-substitution MexB variant were cultured in medium containing 0.01–2.56 μg/mL Chl. As expected, cell growth was inhibited by Chl in all strains, but the extent of inhibition differed among the MexB variants. In particular, cells expressing the Q125E variant exhibited reduced growth even at the lowest Chl concentration tested among all variants.Cells expressing the S180A, Q273E, and R128E variants also exhibited substantially reduced growth compared with wild-type MexB.

We next examined whether these amino acid substitutions also affected resistance to other MexB substrates, namely minocycline, levofloxacin, and CYMAL-7. As in the case of Chl, the Q125E variant caused the most severe reduction in cell growth in the presence of these substrates, indicating that Q125 plays a key role in MexB-mediated resistance to multiple compounds.

4.1 Material and Methods

4.1.1 Preparation of MexB mutants

Plasmids encoding MexB variants were constructed by PCR-based site-directed mutagenesis using PrimeSTAR GXL DNA polymerase and a pGEM-T Easy vector harboring *mexA*Δ736–*mexB* as the template. The sequences of the primers used for PCR are listed in Table 4.1.1. PCR was carried out according to the standard protocol for PrimeSTAR GXL, using 25 cycles of denaturation at 98°C for 10 s and extension at 68°C for 8 min. To remove the residual template plasmid, 25 μL of the PCR product was mixed with 1 μL DpnI and 3 μL 10× CutSmart buffer, and the volume was adjusted to 30 μL with sterile water, followed by incubation at 37°C for 1 h.

For transformation, 3 μL of the DpnI-treated plasmid solution was added to 27 μL XL10-Gold competent cells, and heat shock was performed at 42°C for 45 s. The transformed cells were diluted in 270 μL SOC medium and allowed to recover at 37°C for 1 h with shaking. After recovery, 150 μL of the culture was spread onto LB agar plates containing ampicillin (100 μg/mL) and incubated overnight at 37°C. Single colonies were inoculated into 3 mL LB medium containing ampicillin (100 μg/mL) and cultured overnight at 37°C with shaking. Cells were harvested, and plasmid DNA of the pGEM-*mexA*Δ736–*mexB* variants was purified. For each 10 μL aliquot of pGEM-mexAΔ738–mexB mutant plasmid, 1 μL SmaI, 1 μL NdeI, and 1.5 μL 10× CutSmart buffer were added, and the volume was adjusted to 15 μL with sterile water. The reaction mixtures were then incubated at 37°C for 1 h.

Similarly, 25 μL of pMMB67HE-mexA-mexB-oprM plasmid were mixed with 1 μL SmaI, 1 μL NdeI, and 3 μL 10× CutSmart buffer and incubated at 37°C for 1 h. The restriction enzyme–digested plasmids were separated by electrophoresis on a 1.0%

agarose gel, and the DNA bands corresponding to the desired fragments were excised and purified. The restriction enzyme–digested plasmids were separated by electrophoresis on a 1.0% agarose gel, and the DNA bands corresponding to the desired fragments were excised and purified. The purified DNA fragments were then ligated into the pMMB67HE vector using T4 DNA ligase. An aliquot (1 μL) of the ligation mixture was added to 29 μL XL10-Gold competent cells, and transformation was performed by heat shock at 42°C for 45 s. The transformed cells were diluted with 270 μL SOC medium and allowed to recover at 37°C for 1 h with shaking. After recovery, 150 μL of the culture was spread onto LB agar plates containing ampicillin (100 μg/mL) and incubated at 37°C. Single colonies were inoculated into 3 mL LB medium containing ampicillin (100 μg/mL) and cultured overnight at 37°C with shaking. Cells were harvested, and plasmid DNA of the pMMB67HE-*mexA-mexB-oprM* encoding MexB variants were purified.

Table 4.1.1 Lists of primers used in this study.

Primer name	Sequences (5'-3')
MexB_Q125E_Forward	GAAGTGCAGCGCGAAGGGATCCGGGTG
MexB_Q125E_Reverse	CACCCGGATCCCTTCGCGCTGCACTTC
MexB_R128E_Forward	CAGCGCCAGGGGATCGAAGTGACCAAG GCG GTG
MexB_R128E_Reverse	CACCGCCTTGGTCACTTCGATCCCCTGGCGCTG
MexB_F178Y_Forward	GGCGTCGGTGACTATCAGGTGTTCGGC
MexB_F178Y_Reverse	GCCGAACACCTGATAGTCACCGACGCC
MexB_F178W_Forward	GGCGTCGGTGACTGGCAGGTGTTC
MexB_F178W_Reverse	GAACACCTGCCAGTCACCGACGCC
MexB_F178A_Forward	GTGACTTCCAGGTGGCCGGCTCGCAGTAC
MexB_F178A_Reverse	GTACTGCGAGCCGGCCACCTGGAAGTCAC
MexB_G179A_Forward	TTCCAGGTGTTCGCATCGCAGTACTCG
MexB_G179A_Reverse	CGAGTACTGCGATGCGAACACCTGGAA
MexB_S180A_Forward	CAGGTGTTCGGCGCACAGTACTCGATG
MexB_S180A_Reverse	CATCGAGTACTGTGCGCCGAACACCTG
MexB_Q273E_Forward	GTAGGCCTGGGCGGCGAAGACTACAGCATCAAC
MexB_Q273E_Reverse	GTTGATGCTGTAGTCTTCGCCGCCCAGGCCTAC

4.1.2 In vitro chloramphenicol resistance assay

Aliquots (1 μL) of each pMMB67HE-mexA-mexB-oprM plasmid encoding a MexB variant were added to 27 μL of *E. coli* C43(DE3) Δ*acrAB* Δ*tolC* competent cells, and transformation was performed by heat shock at 42°C for 45 s. The transformed cells were diluted with 270 μL SOC medium and allowed to recover at 37°C for 1 h with shaking. After recovery, 150 μL of the culture was spread onto LB agar plates containing ampicillin (100 μg/mL) and incubated at 37°C. Single colonies were inoculated into 3 mL LB medium containing ampicillin (100 μg/mL) and cultured overnight at 37°C with shaking. Cultures were adjusted to an OD590 of 1.0 in LB. Each adjusted culture medium 4 μL were spotted onto LB agar plates supplemented with 100 μg/mL ampicillin and 0.01–2.56 μg/mL chloramphenicol. Plates were incubated at 37°C for 12 h. Control plates lacking chloramphenicol were processed in parallel.

Colony growth intensities were quantified using ImageJ. For normalization, growth on chloramphenicol-free medium for each strain was set to 1, and relative growth on chloramphenicol-containing plates was calculated accordingly. Differences between the WT MexB strain and each variant strain were evaluated using two-sided Welch's t-tests.

4.1.3 In vitro minocycline resistance assay

Experiments were performed using the pMMB67HE-*mexA-mexB-oprM* plasmids encoding MexB variants generated in Section 4.1. Transformation of competent E. coli C43(DE3) Δ*acrAB* Δ*tolC* cells with these plasmids was carried out as described in Section 4.2.1. Single colonies were inoculated into 3 mL LB medium containing ampicillin (100 μg/mL) and cultured overnight at 37°C with shaking. Cultures were adjusted to an OD590 of 1.0 in LB. Each adjusted culture medium 4 μL were spotted onto LB agar plates supplemented with 100 μg/mL ampicillin and 0.005–0.16 μg/mL minocycline. Plates were incubated at 37°C for 12 h. Control plates lacking minocycline were processed in parallel.

4.1.4 In vitro levofloxacin resistance assay

Experiments were performed using the pMMB67HE-*mexA-mexB-oprM* plasmids encoding MexB variants generated in Section 4.1. Transformation of competent *E. coli* C43(DE3) Δ*acrAB* Δ*tolC* cells with these plasmids was carried out as described in Section 4.2.1. Single colonies were inoculated into 3 mL LB medium containing ampicillin (100 μg/mL) and cultured overnight at 37°C with shaking. Cultures were adjusted to an OD590 of 1.0 in LB. Each adjusted culture medium 4 μL were spotted onto LB agar plates supplemented with 100 μg/mL ampicillin and 0.0001–0.0128

μg/mL levofloxacin. Plates were incubated at 37°C for 12 h. Control plates lacking levofloxacin were processed in parallel.

4.1.5 In vitro CYMAL-7 resistance assay

Experiments were performed using the pMMB67HE-*mexA-mexB-oprM* plasmids encoding MexB variants generated in Section 4.1. Transformation of competent E. coli C43(DE3) Δ*acrAB* Δ*tolC* cells with these plasmids was carried out as described in Section 4.2.1. Single colonies were inoculated into 3 mL LB medium containing ampicillin (100 μg/mL) and cultured overnight at 37°C with shaking. Cultures were adjusted to an OD590 of 1.0 in LB. Each adjusted culture medium 4 μL were spotted onto LB agar plates supplemented with 100 μg/mL ampicillin and 1.95–62.5 μg/mL CYMAL-7. Plates were incubated at 37°C for 12 h. Control plates lacking CYMAL-7 were processed in parallel.

4.2 Result

4.2.1 In vitro chloramphenicol resistance assay of MexB variants

To validate DBP residues responsible for Chl recognition identified by structure analysis, we prepared single substitution MexB variants (Q125E, R128E, F178Y/W/A, G179A, S180A, Q273E) and assessed susceptibility in Chl supplemented media. *E. coli*. C43(DE3) Δ*acrAB* Δ*tolC* cells expressing each MexB variant were cultured in 0.01–2.56 μg/mL Chl (Fig.4.2.1.1). At 1.28 μg/mL Chl, growth of WT MexB–expressing cells was markedly reduced, and at 2.56 μg/mL Chl no growth was observed. At concentrations 0.16 μg/mL Chl, cells expressing DBP variants and cells carrying the Δ*mexB* plasmid (vector control) exhibited decreased growth (Table 4.2.1).

At 0.32 μg/mL Chl, cells expressing WT MexB showed no detectable decrease in growth. In contrast, all single-substitution DBP variants exhibited reduced growth, with percent decreases in normalized colony intensity (relative to drug-free controls) of 85% (Q125E), 57% (S180A), 55% (Q273E), 44% (R128E), and 23–40% for the remaining variants (Table 4.2.1, Fig.4.2.1.2). Among residues proximal to Chl, substitutions at Q125 produced the largest decrease, followed by S180 and Q273. Substitutions at R128 F178 and G179 had a smaller effect overall.

Table. 4.2.1 *In vitro* chloramphenicol resistance assay of cells harboring inactive pump (Δ*mexB*), wildtype MexB, and deep binding pocket variants.

	0.01 µg/mL	0.02 µg/mL	0.04 µg/mL	0.08 µg/mL	0.16 µg/mL	0.32 µg/mL	0.64 µg/mL	1.28 µg/mL	2.56 µg/mL
ΔMexB	1.11 ± 0.05	1.08 ± 0.04	1.07 ± 0.04	0.86 ± 0.02 *	0.58 ± 0.19	---	---	---	---
MexB	1.10 ± 0.03	1.07 ± 0.03	1.11 ± 0.04	1.04 ± 0.04	1.08 ± 0.06	0.97 ± 0.05	0.73 ± 0.04	0.24 ± 0.14	---
Q125E	1.12 ± 0.03	1.08 ± 0.05	1.08 ± 0.02	0.95 ± 0.02	0.78 ± 0.06 *	0.15 ± 0.15 *	---	---	---
R128E	1.08 ± 0.03	1.02 ± 0.02	1.00 ± 0.02	0.98 ± 0.07	0.88 ± 0.04 *	0.56 ± 0.05 *	---	---	---
F178Y	1.08 ± 0.04	1.00 ± 0.02	0.99 ± 0.02	0.99 ± 0.07	0.89 ± 0.04 *	0.60 ± 0.04 *	---	---	---
F178W	1.01 ± 0.03	1.01 ± 0.04	1.01 ± 0.02	0.90 ± 0.03	0.87 ± 0.04 *	0.61 ± 0.03 *	---	---	---
F178A	1.02 ± 0.02	0.94 ± 0.03	1.01 ± 0.01	0.93 ± 0.03	0.97 ± 0.03	0.77 ± 0.01 *	0.47 ± 0.06 *	---	---
G179A	1.02 ± 0.02	1.01 ± 0.02	1.00 ± 0.02	0.89 ± 0.04	0.85 ± 0.03 *	0.66 ± 0.02 *	---	---	---
S180A	1.06 ± 0.02	1.04 ± 0.01	1.01 ± 0.02	0.91 ± 0.08	0.73 ± 0.05 *	0.43 ± 0.02 *	---	---	---
Q273E	1.05 ± 0.03	1.03 ± 0.03	1.00 ± 0.02	1.01 ± 0.13	0.78 ± 0.05 *	0.45 ± 0.04 *	---	---	---

Data are shown as mean ± s.e.m. (N = 4 biologically independent replicates). Statistical significance was assessed using two-sided Welch's t-tests; *$p < 0.05$. Cell growth values were normalized to the control (ampicillin). Negative results (pink shading) indicate a reduction in cell growth of ≥15% relative to the control, and darker pink shades correspond to stronger growth inhibition.

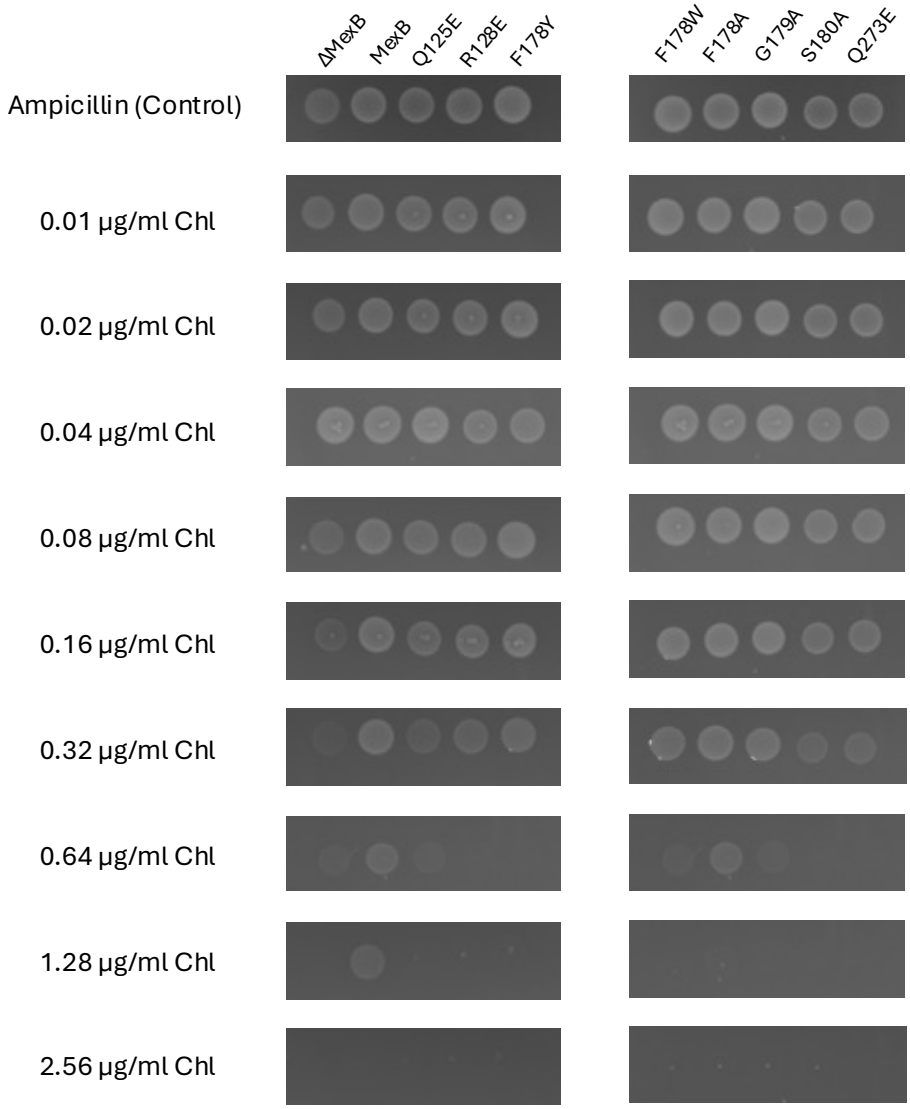

Fig. 4.2.1.1 In vitro chloramphenicol resistance assay of cells harboring inactive pump (Δ*mexB*), wildtype MexB, and deep binding pocket variants (Q125E, R128E, F178Y, F178W, F178A, G179A, S180A, Q273E).

Chloramphenicol resistance assays were performed using *E. coli* C43(DE3) Δ*acrAB* Δ*tolC* harboring pMMB67HE-*mexB* or its variants. Cells were adjusted to an optical density at 590 nm (OD_{590}) of 1.0 and spotted onto LB agar plates containing Chloramphenicol or onto control plates lacking chloramphenicol. Each assay was performed in triplicate.

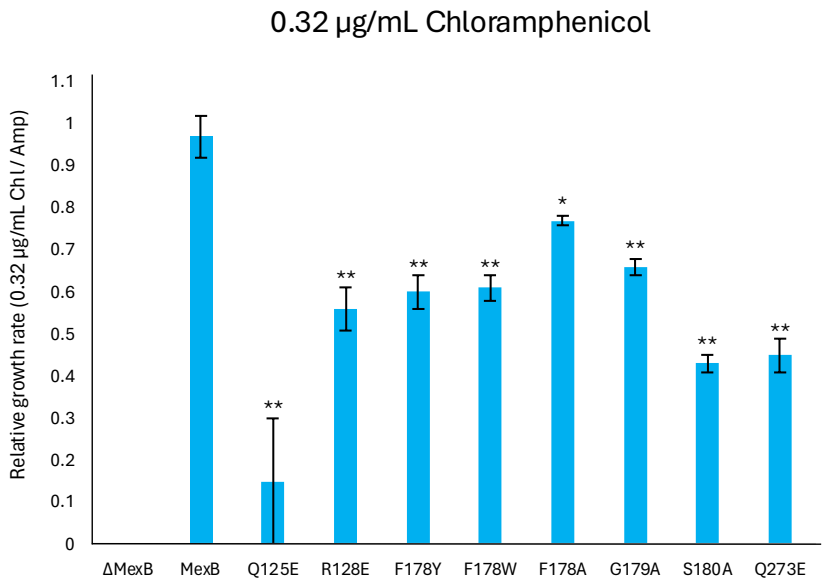

Fig. 4.2.1.2 Cell Growth comparison in the presence of 0.32 µg/mL Chloramphenicol.

Comparison of bacterial growth in the presence of chloramphenicol. *E. coli* harboring plasmids expressing wild-type MexB or DBP-groove mutants were grown on LB agar containing 100 µg/mL ampicillin alone or 100 µg/mL ampicillin with 0.32 µg/mL chloramphenicol. Colony growth was quantified from plate images by measuring colony intensity using ImageJ. Growth ratios were calculated by normalizing the colony intensity on plates containing 100 µg/mL ampicillin with 0.32 µg/mL chloramphenicol to that on plates containing 100 µg/mL ampicillin alone. (*$P < 0.05$, **$P < 0.01$)

4.2.2 In vitro minocycline or levofloxacin resistance assay of MexB variants

At 0.02 μg/mL minocycline, Q125E, S180A, and Q273E showed no detectable growth, whereas R128E showed 83% growth inhibition (Table 4.2.2.1, Fig. 4.2.2.1). For levofloxacin, at 0.0064 μg/mL, Q125E, S180A, and Q273E again showed no detectable growth, while R128E showed 63% inhibition (Table 4.2.2.2, Fig. 4.2.2.2). Consistent with their strong effects on growth at 0.32 μg/mL chloramphenicol (Table 4.2.1), substitution at Q125, which had the strongest effect on Chl-dependent growth, and substitutions at S180 and Q273, which also substantially reduced growth, likewise impaired resistance to both minocycline and levofloxacin. R128 displayed substrate-dependent effects: modest with Chl (44% inhibition at 0.32 μg/mL), greater with levofloxacin (63% inhibition at 0.0064 μg/mL) and pronounced with minocycline (77% inhibition at 0.02 μg/mL).

Table 4.2.2.1 Minocycline resistance assay of MexB DBP mutants

	0.005 μg/mL	0.01 μg/mL	0.02 μg/mL	0.04 μg/mL	0.08 μg/mL	0.16 μg/mL
ΔMexB	0.97 ± 0.04	0.61 ± 0.30	-	-	-	-
MexB	0.96 ± 0.05	0.87 ± 0.06	0.70 ± 0.01	0.58 ± 0.09	0.39 ± 0.20	-
Q125E	0.97 ± 0.02	0.84 ± 0.06	-	-	-	-
R128E	0.95 ± 0.03	0.83 ± 0.04	0.23 ± 0.23	-	-	-
F178Y	1.00 ± 0.04	0.83 ± 0.07	0.59 ± 0.00	-	-	-
F178W	1.01 ± 0.02	0.82 ± 0.07	0.62 ± 0.01	-	-	-
F178A	0.99 ± 0.02	0.97 ± 0.03	0.71 ± 0.02	-	-	-
G179A	0.98 ± 0.03	0.81 ± 0.07	0.62 ± 0.00	-	-	-
S180A	0.95 ± 0.04	0.82 ± 0.03	-	-	-	-
Q273E	0.96 ± 0.02	0.85 ± 0.04	-	-	-	-

Data are shown as mean ± s.e.m. (N = 3 biologically independent replicates). Cell growth values were normalized to the control (ampicillin). Negative results (pink shading) indicate a reduction in cell growth of ≥15% relative to the control, and darker pink shades correspond to stronger growth inhibition.

Table 4.2.2.2 Levofloxacin resistance assay of MexB DBP mutants

	0.0001 μg/mL	0.0002 μg/mL	0.0004 μg/mL	0.0008 μg/mL	0.0016 μg/mL	0.0032 μg/mL	0.0064 μg/mL	0.0128 μg/mL
ΔMexB	1.00 ± 0.04	1.06 ± 0.09	0.96 ± 0.02	0.99 ± 0.04	1.03 ± 0.11	0.95 ± 0.07	-	-
MexB	0.99 ± 0.04	1.07 ± 0.11	1.01 ± 0.04	1.00 ± 0.03	1.04 ± 0.13	1.00 ± 0.10	0.71 ± 0.05	-
Q125E	1.00 ± 0.02	1.11 ± 0.11	1.03 ± 0.04	1.04 ± 0.04	1.03 ± 0.11	0.88 ± 0.06	-	-
R128E	1.01 ± 0.06	1.09 ± 0.12	1.01 ± 0.06	1.01 ± 0.06	1.05 ± 0.14	1.01 ± 0.13	0.37 ± 0.21	-
F178Y	1.02 ± 0.04	1.11 ± 0.10	1.06 ± 0.09	0.99 ± 0.04	1.03 ± 0.12	1.00 ± 0.10	0.64 ± 0.08	-
F178W	1.01 ± 0.02	1.15 ± 0.10	1.14 ± 0.08	1.02 ± 0.03	1.01 ± 0.11	1.01 ± 0.09	0.51 ± 0.18	-
F178A	1.00 ± 0.03	1.10 ± 0.11	1.15 ± 0.08	1.02 ± 0.04	1.05 ± 0.14	1.02 ± 0.11	0.75 ± 0.05	-
G179A	1.07 ± 0.08	1.15 ± 0.11	1.03 ± 0.03	1.02 ± 0.04	1.06 ± 0.13	0.94 ± 0.14	0.74 ± 0.11	-
S180A	0.97 ± 0.04	1.18 ± 0.16	0.99 ± 0.05	0.98 ± 0.06	0.98 ± 0.09	0.88 ± 0.07	-	-
Q273E	0.95 ± 0.03	1.11 ± 0.12	0.95 ± 0.02	0.95 ± 0.02	0.96 ± 0.08	0.87 ± 0.05	-	-

Data are shown as mean ± s.e.m. (N = 4 biologically independent replicates). Cell growth values were normalized to the control (ampicillin). Negative results (pink shading) indicate a reduction in cell growth of ≥15% relative to the control, and darker pink shades correspond to stronger growth inhibition.

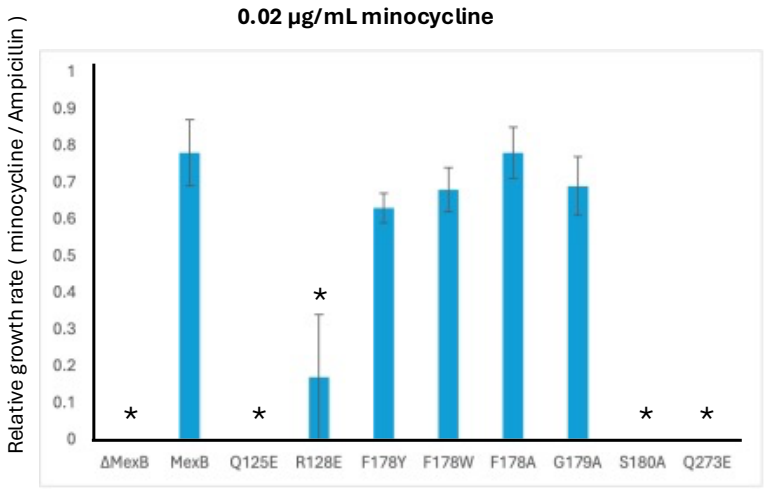

Fig. 4.2.2.1 Cell Growth comparison in the presence of 0.02 μg/mL minocycline.

Comparison of bacterial growth in the presence of minocycline. *E. coli* harboring plasmids expressing wild-type MexB or DBP-groove mutants were grown on LB agar containing 100 μg/mL ampicillin alone or 100 μg/mL ampicillin with 0.02 μg/mL minocycline. Colony growth was quantified from plate images by measuring colony intensity using ImageJ. Growth ratios were calculated by normalizing the colony intensity on plates containing 100 μg/mL ampicillin with 0.02 μg/mL minocycline to that on plates containing 100 μg/mL ampicillin alone. (*$P < 0.05$)

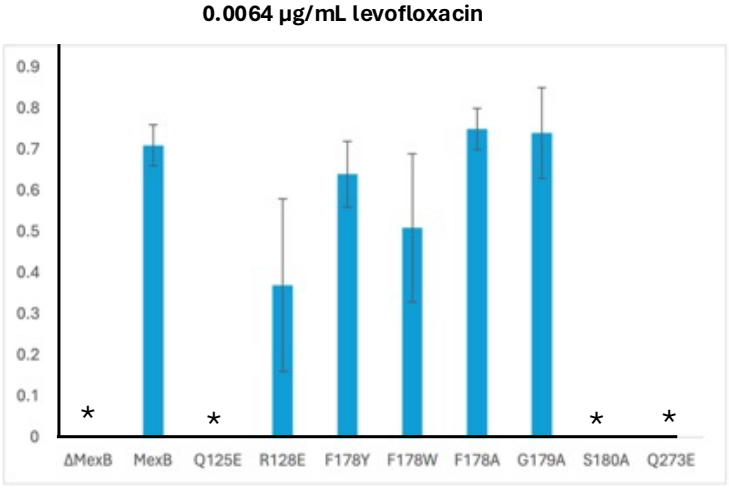

Fig. 4.2.2.2 Cell Growth comparison in the presence of 0.0064 μg/mL levofloxacin.

Comparison of bacterial growth in the presence of levofloxacin. *E. coli* harboring plasmids expressing wild-type MexB or DBP-groove mutants were grown on LB agar containing 100 μg/mL ampicillin alone or 100 μg/mL ampicillin with 0.0064 μg/mL levofloxacin. Colony growth was quantified from plate images by measuring colony intensity using ImageJ. Growth ratios were calculated by normalizing the colony intensity on plates containing 100 μg/mL ampicillin with 0.0064 μg/mL levofloxacin to that on plates containing 100 μg/mL ampicillin alone. (*$P < 0.05$)

4.2.3 In vitro CYMAL-7 resistance assay of MexB variants

The contribution of DBP residues to CYMAL-7 efflux was assessed. Cells expressing WT MexB grew at ≥62.5 μg/mL CYMAL-7, whereas cell expressing any of single-substitution DBP variants cells expressing any of the DBP single-substitution variants (Q125E, R128E, F178Y/W/A, G179A, S180A, Q273E) showed complete growth inhibition at 31.2 μg/mL CYMAL-7. This result suggests that all DBP variants may be important for CYMAL-7 efflux (Fig. 4.2.3).

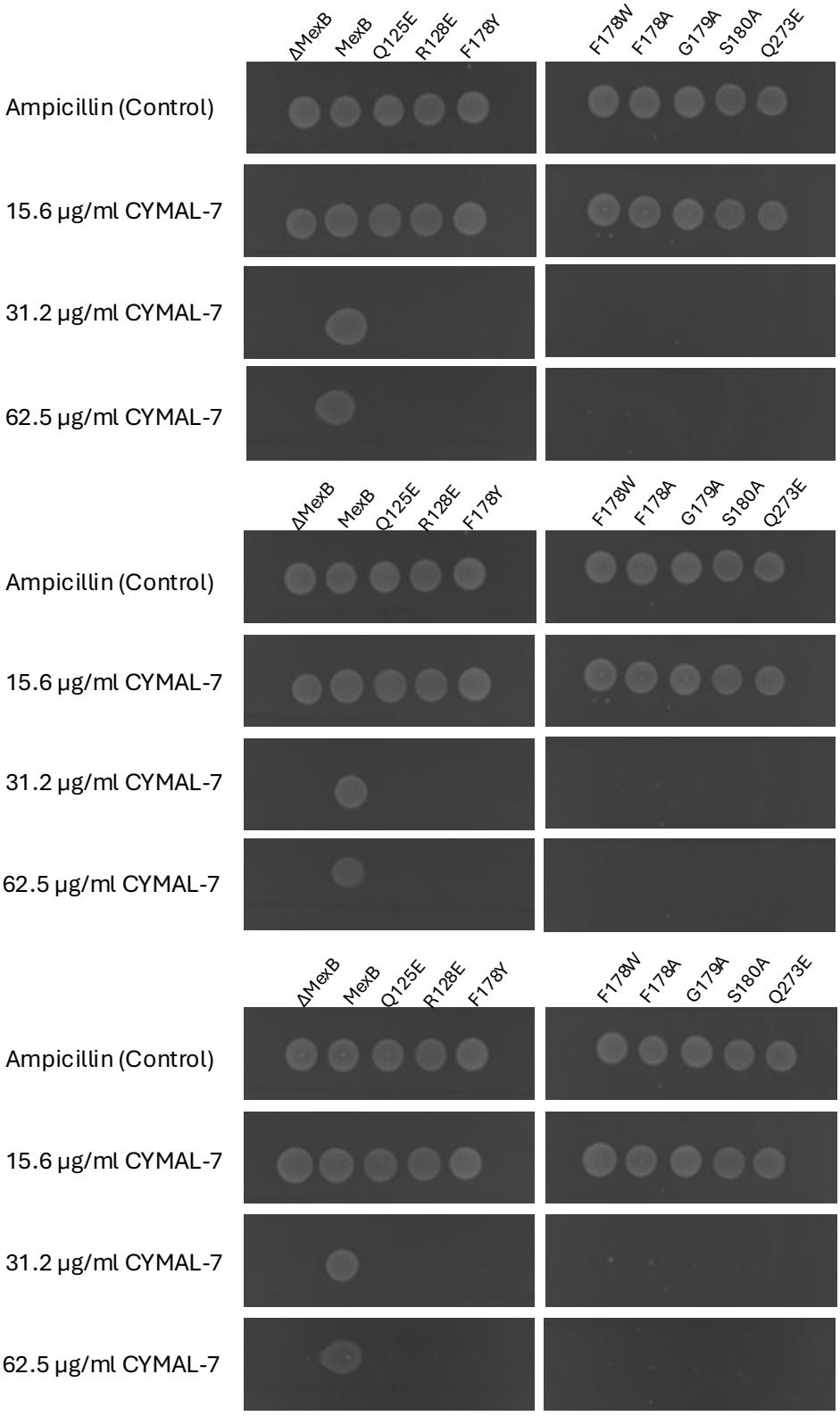
ΔMexB
MexB
Q125E
R128E
F178Y
F178W
F178A
G179A
S180A
Q273E
Ampicillin (Control)
15.6 μg/ml CYMAL-7
31.2 μg/ml CYMAL-7
62.5 μg/ml CYMAL-7
ΔMexB
MexB
Q125E
R128E
F178Y
F178W
F178A
G179A
S180A
Q273E
Ampicillin (Control)
15.6 μg/ml CYMAL-7
31.2 μg/ml CYMAL-7
62.5 μg/ml CYMAL-7
ΔMexB
MexB
Q125E
R128E
F178Y
F178W
F178A
G179A
S180A
Q273E
Ampicillin (Control)
15.6 μg/ml CYMAL-7
31.2 μg/ml CYMAL-7
62.5 μg/ml CYMAL-7

Fig. 4.2.3 *In vitro* substrate resistance assay of cells harboring inactive pump (Δ*mexB*), wildtype MexB, and deep binding pocket variants (Q125E, R128E, F178Y, F178W, F178A, G179A, S180A, Q273E).

CYMAL-7 resistance assays were performed using *E. coli* C43(DE3) Δ*acrAB* Δ*tolC* harboring pMMB67HE-*mexA-mexB-oprM* or *mexB* variants. Cells were adjusted to an optical density at 590 nm (OD_{590}) of 1.0 and spotted onto LB agar plates containing CYMAL-7 or onto control plates lacking CYMAL-7. Each assay was performed in triplicate.

Chapter5

Discussion and conclusion

5.1 Discussion

Chloramphenicol (Chl) is positioned at the deep end of the DBP groove (Fig. 3.2.3.1A, B), at a site distinct from those reported for drug-bound AcrB structures (35,36). The ligand position overlaps with the maltoside headgroups of DDM and LMNG (Fig. 3.2.3.3). In the Chl-bound MexB structure determined in this study, we identified residues involved in Chl binding. Based on these structural information, single-substitution DBP variants of MexB (Q125E, R128E, F178Y, F178W, F178A, G179A, S180A, and Q273E) were prepared. In the presence of Chl, Q125E markedly decreased cell growth, whereas R128E, S180A, and Q273E produced moderate decreases. By contrast, the effects of the F178 variants were small. This pattern is consistent with the structural observation that Chl binding is stabilized by hydrogen bonding rather than π–π stacking. In the presence of minocycline and levofloxacin, Q125E, S180A, and Q273E also markedly decreased cell growth, and R128E caused additional reductions with both drugs. In AcrB reference structures, minocycline and levofloxacin bind within the DBP, where they approach residues equivalent to S180 and Q273 but not the Q125-equivalent position (Fig.3.2.3.2). This result suggests that S180 and Q273 in MexB are likely to contribute, at least in part, through direct contacts with DBP-binding antibiotics, whereas Q125, despite not forming obvious contacts in the AcrB complexes, influences efflux from its exit-proximal position. Together with the marked decreases in drug resistance caused by Q125E to chloramphenicol, minocycline, and levofloxacin,

these findings raise the possibility that Q125 acts as an exit-proximal residue that is important for the efflux of substrate, likely interacting with substrates as they progress from the DBP toward the exit gate.

Taken together, these results indicate that Q125, R128, S180, and Q273 are indispensable for MexB-mediated resistance to chloramphenicol, minocycline, levofloxacin, and CYMAL-7, and that they form a common subsite in the DBP groove that is contacted by chemically diverse substrates. Among these residues, however, the Q125E substitution caused the most severe loss of resistance, identifying this position as the primary residue within the subsite. Consistent with this view, substitutions that introduce an acidic side chain into the same subsite, R128E and Q273E, also reduced MexB-mediated resistance, most likely because the additional negative charges perturb the electrostatic environment in the distal pocket and destabilize ligand binding. A similar result has been reported for AdeB, in which the N276D substitution, located near the position of MexB residue Q273 in the distal binding pocket, decreased resistance to chloramphenicol, levofloxacin, and minocycline, whereas the E89Q mutant increased resistance to these drugs (35). These observations suggest that modest changes in side-chain charge within this region can affect efflux activity.

The DBP groove of MexB comprises eight hydrophobic and nine polar residues, whereas that of AdeB comprises nine hydrophobic and eight polar residues, indicating that the DBP groove of AdeB is slightly more hydrophobic than that of MexB. In AdeB, the A180S substitution increased resistance to minocycline, whereas in MexB the S180A mutation decreased resistance to this drug, suggesting that recognition of minocycline within the DBP groove is mediated by polar residues. In contrast, the A180S substitution in AdeB and the S180A substitution in MexB both reduced

resistance to chloramphenicol and levofloxacin. These observations suggest that, in the recognition of chloramphenicol and levofloxacin, differences in DBP groove polarity and hydrophobicity may give rise to distinct substrate-binding modes among RND pumps.

We therefore focused on Q125 as the key residue within this MexB subsite and examined how the Q125-equivalent position is configured in other RND transporters (Fig. 5.1). A comparison of primary sequences from 47 transporters revealed that glutamine occupies the Q125-equivalent position in 24 of these 47 RND transporters, whereas glutamate was never observed and aspartate appeared only in MexY and AmrB. When glutamine is not present, this position is most commonly occupied by hydrophobic residues such as leucine (7 of 47) or proline (5 of 47). Thus, glutamine is the predominant residue at the Q125-equivalent position, and acidic residues at this site appear to be extremely rare, indicating that a non-acidic environment is strongly preferred. These observations suggest that, in those RND transporters that retain a glutamine at the position equivalent to MexB Q125, this residue may provide a recognition site for antibiotics and other substrates like that identified in MexB. How alternative residues such as leucine or proline modulate the properties of this site remains unclear and will require future structural and functional analyses.

We have identified a ligand-binding site within the DBP groove of MexB that is used for antibiotic recognition. However, the substrate specificity of MexB is likely to arise from the concerted action of multiple structural elements within this transporter, including the DBP, the PBP, the Gate-loop, and the multiple channels. Thus, future structural analyses of MexB in complex with different substrates, in combination with

functional studies focusing on the binding sites and transport channels, should provide a more comprehensive understanding of how MexB achieves multidrug recognition.

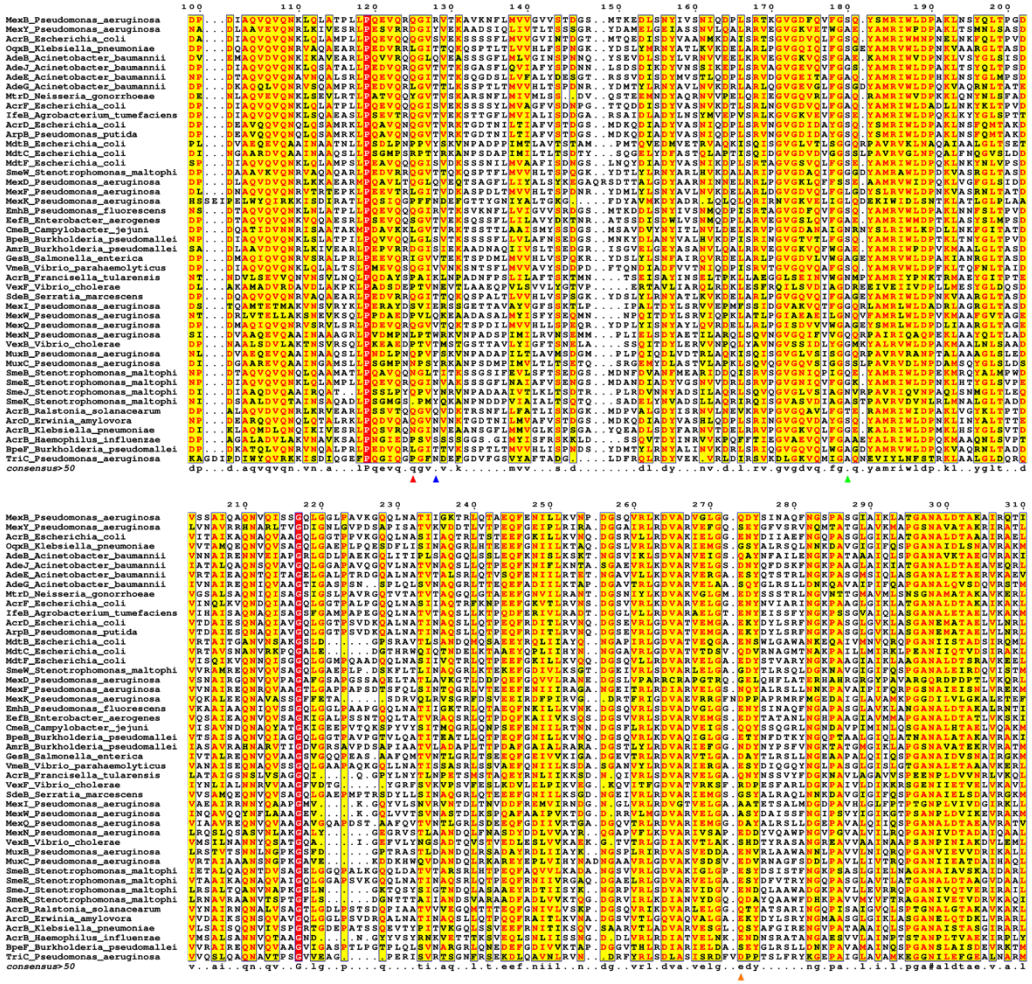

Fig. 5.1 Comparison of the primary sequences of 47 RND transporters.

Residues corresponding to MexB positions 125, 128, 180, and 273 are indicated by red, blue, green, and orange arrows, respectively.

5.2 Conclusion

Pseudomonas aeruginosa harbors the RND-type tripartite multidrug efflux pump MexAB–OprM, which exports a broad range of antibacterial compounds and is a major contributor to multidrug resistance that complicates the treatment of severe hospital-acquired infections. Although X-ray crystal structures of MexB have been reported, antibiotic-bound structures had remained largely unavailable. In this study, we determined the structure of drug-free MexB at 2.30 Å resolution and the structure of chloramphenicol-bound MexB at 2.89 Å resolution by X-ray crystallography. Chloramphenicol-bound MexB formed an asymmetric trimer, in which the three protomers corresponded to the Access, Binding, and Extrusion states. Ligand electron density was observed only in the distal binding pocket (DBP) of the Binding protomer. Chloramphenicol occupied the DBP groove, at a position distinct from binding sites reported in antibiotic-bound AcrB structures. In the complex, chloramphenicol interacted primarily with six residues in MexB: Q125, R128, F178, G179, S180, and Q273.

Guided by these structural observations, we generated single-substitution variants in the DBP groove (Q125E, R128E, F178Y, F178W, F178A, G179A, S180A, and Q273E) and quantified growth under antibiotic pressure. In the presence of chloramphenicol, Q125E caused a pronounced reduction in growth, whereas R128E, S180A, and Q273E produced moderate decreases. By contrast, the effects of the F178 variants were relatively small. This pattern is consistent with the structural observation that chloramphenicol binding is stabilized predominantly by hydrogen-bonding interactions rather than by π–π stacking.

To assess whether DBP groove residues important for chloramphenicol recognition also contribute to the recognition of other DBP-binding antibiotics, we quantified growth in the presence of minocycline and levofloxacin, both of which are MexB substrates and have been structurally characterized in complex with the DBP of the homologous transporter AcrB. In AcrB, minocycline binds in the DBP groove via interactions with hydrophobic residues such as F178 and F615, as well as polar residues including S180, E273, and N274 (18). Levofloxacin binds within the DBP cave and interacts with hydrophobic side chains of AcrB residues such as F178, F610, and F615 (17). For both antibiotics, clear contacts with Q125 have not been reported.

Functionally, under both minocycline and levofloxacin conditions, Q125E, S180A, and Q273E markedly reduced growth. These results suggest that Q125 can influence the transport (efflux) process from an exit-proximal position, even in cases where direct ligand contacts are not apparent in available AcrB complexes. Together with the pronounced loss of resistance conferred by Q125E against chloramphenicol, minocycline, and levofloxacin, our findings raise the possibility that Q125 functions as an important exit-proximal residue and may engage substrates as they progress from the DBP toward the exit gate.

Overall, we identified a ligand-binding site within the MexB DBP groove that contributes to antibiotic recognition. However, MexB substrate specificity is likely to arise from the coordinated contributions of multiple structural elements within the transporter, including the DBP, the proximal binding pocket (PBP), the gate loop, and multiple transport channels. Future studies combining structures of MexB in complex with diverse substrates with functional analyses focused on binding sites and transport

pathways should provide a more comprehensive understanding of how MexB achieves multidrug recognition.

Reference

1. Pang, Z., Raudonis, R., Glick, B.R., Lin, T.-J., and Cheng, Z. (2019) Antibiotic resistance in Pseudomonas aeruginosa: mechanisms and alternative therapeutic strategies. Biotechnol. Adv. 37, 177–192.
2. Li, X.-Z., Plésiat, P., and Nikaido, H. (2015) The challenge of efflux-mediated antibiotic resistance in Gram-negative bacteria. Clin. Microbiol. Rev. 28, 337–418.
3. Tseng, T.T., Gratwick, K.S., Kollman, J., Park, D., Nies, D.H., Goffeau, A., and Saier, M.H., Jr. (1999) The RND permease superfamily: an ancient, ubiquitous and diverse family that includes human disease and development proteins. J. Mol. Microbiol. 1, 107–125.
4. Koronakis V, Sharff AJ, Koronakis E, Luisi B, Hughes C. (200) Crystal structure of the bacterial membrane protein TolC central to multidrug efflux and protein export. Nature.405, 914-919.
5. Du, D., Wang, Z., James, N. *et al.* (2014) Structure of the AcrAB–TolC multidrug efflux pump. *Nature* 509, 512–515.
6. K. Poole. (2004) Efflux-mediated multiresistance in Gram-negative bacteria. Clin Microbiol Infect. 10, 12–26
7. Masuda N, Sakagawa E, Ohya S, Gotoh N, Tsujimoto H, Nishino T. (2004) Substrate specificities of MexAB-OprM, MexCD-OprJ, and MexXY-oprM efflux pumps in Pseudomonas aeruginosa. Antimicrob Agents Chemother. 44, 3322-3327

8. Okamoto K, Gotoh N, Nishino T. (2002) Alterations of susceptibility of Pseudomonas aeruginosa by overproduction of multidrug efflux systems, MexAB-OprM, MexCD-OprJ, and MexXY/OprM to carbapenems: substrate specificities of the efflux systems. J Infect Chemother. 8, 371-373
9. Li XZ, Zhang L, Srikumar R, Poole K. (1998) Beta-lactamase inhibitors are substrates for the multidrug efflux pumps of Pseudomonas aeruginosa. Antimicrob Agents Chemother.42, 399-403
10. Phan, G., Benabdelhak, H., Lascombe, M.-B., Benas, P., Rety, S., Picard, M., Ducruix, A., Etchebest, C., and Broutin, I. (2010) Structural and dynamical insights into the opening mechanism of P. aeruginosa OprM channel. Structure 18, 507–517.
11. Sennhauser, G., Bukowska, M.A., Briand, C., and Grütter, M.G. (2009) Crystal structure of the multidrug exporter MexB from Pseudomonas aeruginosa. J. Mol. Biol. 389, 134–145.
12. Akama, H., Matsuura, T., Kashiwagi, S., Yoneyama, H., Narita, S., Tsukihara, T., Nakagawa, A., and Nakae, T. (2004) Crystal structure of the membrane fusion protein, MexA, of the multidrug transporter in Pseudomonas aeruginosa. J. Biol. Chem. 279, 25939–25942.
13. Murakami, S., Nakashima, R., Yamashita, E., Matsumoto, T., and Yamaguchi, A. (2006) Crystal structures of a multidrug transporter reveal a functionally rotating mechanism. Nature 443, 173–179.
14. Guan, L., and Nakae, T. (2001) Identification of essential charged residues in transmembrane segments of the multidrug transporter MexB of Pseudomonas aeruginosa. J. Bacteriol. 183, 1734–1739.

15. Su, C.-C., Yin, L., Kumar, N., Dai, L., Radhakrishnan, A., Bolla, J.R., Lei, H.-T., Chou, T.-H., Delmar, J.A., Rajashankar, K.R., Zhang, Q., Shin, Y.-K., and Yu, E.W. (2017) Structures and transport dynamics of a Campylobacter jejuni multidrug efflux pump. Nat. Commun. 8, 171.
16. Morgan, C.E., Glaza, P., Leus, I.V., Trinh, A., Su, C.-C., Cui, M., Zgurskaya, H.I., and Yu, E.W. (2021) Cryoelectron microscopy structures of AdeB illuminate mechanisms of simultaneous binding and exporting of substrates. mBio 12, e03690-20.
17. Nakashima, R., Sakurai, K., Yamasaki, S., Nishino, K., and Yamaguchi, A. (2011) Structures of the multidrug exporter AcrB reveal a proximal multisite drug-binding pocket. Nature 480, 565–569.
18. Sennhauser, G., Amstutz, P., Briand, C., Storchenegger, O., and Grütter, M.G. (2007) Drug export pathway of multidrug exporter AcrB revealed by DARPin inhibitors. PLoS Biol. 5, e7
19. Zwama, M.M., Yamasaki, S., Nakashima, R., Sakurai, K., Nishino, K., and Yamaguchi, A. (2018) Multiple entry pathways within the efflux transporter AcrB contribute to multidrug recognition. Nat. Commun. 9, 124.
20. Tam, H.K., Foong, W.E., Oswald, C., Herrmann, A., Zeng, H., and Pos, K.M. (2021) Allosteric drug transport mechanism of multidrug transporter AcrB. Nat. Commun. 12, 3889.
21. Nakashima, R., Sakurai, K., Yamasaki, S., Nishino, K., and Yamaguchi, A. (2013) Structural basis for the inhibition of bacterial multidrug exporters. Nature 500, 102–106.

22. Sakurai, K., Yamasaki, S., Nakao, K., Nishino, K., Yamaguchi, A., and Nakashima, R. (2019) Crystal structures of multidrug efflux pump MexB bound with high-molecular-mass compounds. Sci. Rep. 9, 4359.
23. Tsutsumi, K., Yonehara, R., Ishizaka-Ikeda, E., Miyazaki, N., Maeda, S., Iwasaki, K., Nakagawa, A., and Yamashita, E. (2019) Structures of the wild-type MexAB–OprM tripartite pump reveal its complex formation and drug efflux mechanism. Nat. Commun. 10, 1520.
24. Yamashita, E. and Nakagawa, A. (2019) SPring-8 BL44XU, a synchrotron radiation beamline for biological macromolecular assemblies, operated by the Institute for Protein Research, Osaka University. *Biophys. Rev.* 11, 521–523.
25. Higashiura, A., Yamashita, E., Yoshimura, M., Hasegawa, K., Furukawa, Y., Kumasaka, T., Ueno, G., Yamamoto, M., Tsukihara, T., and Nakagawa, A. (2016) SPring-8 BL44XU, beamline designed for structure analysis of large biological macromolecular assemblies. *AIP Conf. Proc.* 1741, 030028.
26. Vonrhein, C., Flensburg, C., Keller, P., Sharff, A., Smart, O., Paciorek, W., Womack, T., and Bricogne, G. (2011) Data processing and analysis with the autoPROC toolbox. *Acta Crystallogr. D Biol. Crystallogr.* 67, 293–302.
27. Kabsch, W. (2010) XDS. *Acta Crystallogr. D Biol. Crystallogr.* 66, 125–132.
28. Adams, P.D., Afonine, P.V., Bunkóczi, G., Chen, V.B., Davis, I.W., Echols, N., Headd, J.J., Hung, L.-W., Kapral, G.J., Grosse-Kunstleve, R.W., McCoy, A.J., Moriarty, N.W., Oeffner, R., Read, R.J., Richardson, D.C., Richardson, J.S., Terwilliger, T.C., and Zwart, P.H. (2010) PHENIX: a comprehensive Python-based system for macromolecular structure solution. *Acta Crystallogr. D Biol. Crystallogr.* 66, 213–221.

29. McCoy, A.J., Grosse-Kunstleve, R.W., Adams, P.D., Winn, M.D., Storoni, L.C., and Read, R.J. (2007) Phaser crystallographic software. *J. Appl. Crystallogr.* 40, 658–674.

30. Emsley, P., Lohkamp, B., Scott, W.G., and Cowtan, K. (2010) Features and development of Coot. *Acta Crystallogr. D Biol. Crystallogr.* 66, 486–501.

31. Afonine, P.V., Grosse-Kunstleve, R.W., Echols, N., Headd, J.J., Moriarty, N.W., Mustyakimov, M., Terwilliger, T.C., Urzhumtsev, A., Zwart, P.H., and Adams, P.D. (2012) Towards automated crystallographic structure refinement with phenix.refine. *Acta Crystallogr. D Biol. Crystallogr.* 68, 352–367.

32. Liebschner, D., Afonine, P.V., Moriarty, N.W., Poon, B.K., Sobolev, O.V., Terwilliger, T.C., and Adams, P.D. (2017) Polder maps: improving OMIT maps by excluding bulk solvent. *Acta Crystallogr. D Struct. Biol.* 73, 148–157.

33. Winn, M.D., Ballard, C.C., Cowtan, K.D., Dodson, E.J., Emsley, P., Evans, P.R., Keegan, R.M., Krissinel, E.B., Leslie, A.G.W., McCoy, A., McNicholas, S.J., Murshudov, G.N., Pannu, N.S., Potterton, E.A., Powell, H.R., Read, R.J., Vagin, A., and Wilson, K.S. (2011) Overview of the CCP4 suite and current developments. *Acta Crystallogr. D Biol. Crystallogr.* 67, 235–242.

34. Otwinowski, Z., and Minor, W. (1997) Processing of X-ray diffraction data collected in oscillation mode. *Methods Enzymol.* 276, 307–326.

35. Ornik-Cha, A., Wilhelm, J., Kobylka, J., Sjuts, H., Vargiu, A.V., Malloci, G., Reitz, J., Seybert, A., Frangakis, A.S., and Pos, K.M. (2021) Structural and functional analysis of the promiscuous AcrB and AdeB efflux pumps suggests different drug binding mechanisms. Nat. Commun. 12, 6919.

36. Eicher, T., Cha, H.J., Seeger, M.A., Brandstätter, L., El-Delik, J., Bohnert, J.A., Kern, W.V., Verrey, F., Grütter, M.G., Diederichs, K., and Pos, K.M. (2012) Transport of drugs by the multidrug transporter AcrB involves an access and a deep binding pocket that are separated by a switch-loop. Proc. Natl. Acad. Sci. USA 109, 5687–5692.